Nuclear shell structures in terms of classical periodic orbits

Ken-ichiro Arita

Department of Physics, Nagoya Institute of Technology, Nagoya 466-8555, Japan

E-mail: arita@nitech.ac.jp

Submitted: 31 October 2015, revised: 20 April 2016

Abstract

Semiclassical periodic-orbit theory (POT) is applied to the physics of nuclear structures, with the use of a realistic nuclear mean-field model given by the radial power-law potential. Evolution of deformed shell structures, which are responsible for various nuclear deformations, are clearly understood from the contribution of short classical periodic orbits (POs). Bifurcations of short POs, which imply underlying local dynamical symmetry, play significant role there. The effect of the spin degree of freedom is also investigated in relevance to the pseudospin symmetry in spherical nuclei and the prolate-oblate asymmetry in shell structures of nuclei with quadrupole-type deformations.

PACS numbers: 21.60.-n, 36.40.-c, 03.65.Sq, 05.45.Mt

arXiv:1603.04316v2 [nucl-th] 6 May 2016

1. Introduction

Independent-particle picture is one of the most important discoveries in the history of nuclear structure physics [1, 2]. Because of dominance of the single-particle motion in nuclear dynamics, various low-energy (near-yrast) properties of nuclei are determined by the characters of the single-particle spectra. Therefore, it is very important to understand the properties of the quantized independent-particle motion in the nuclear mean-field potentials. In general, distribution of the single-particle energy eigenvalues shows a regularly oscillating gross structure, called *shell structure* and, occasionally, a modulation in its amplitude into various kinds of beating patterns called *supershell structure*. Those structures are quite sensitive to the shapes of the potentials. As is well known, such gross structures in the quantum fluctuations play important roles in characterizing the properties of many-fermion systems like nuclei and microclusters. However, the origins of such gross structures are not clear from purely quantum mechanical viewpoints.

Semiclassical theory provides us useful tools to investigate those remarkable gross shell structures in quantum dynamics. It describes the properties of quantum systems in terms of the classical dynamics. Speaking of a classical-quantum correspondence, one may first think about the Ehrenfest theorem, which tells that the expectation values of quantum operators obey the classical equations of motion. Moreover, the individual quantum states also have a close relation to the classical dynamics. In this relevance, one may recall the Bohr-Sommerfeld quantization rule for a particle in one-dimensional potential well $V(x)$, where the energy eigenvalues $\{e_n\}$ are determined by the condition that the action integral along once around the classical orbit to be multiples of the Planck's constant h:

$$2\int_{x_1}^{x_2} p(x;e_n)\mathrm{d}x = nh, \quad n = 1, 2, \cdots . \tag{1}$$

Here, $p(x;e) = \sqrt{2m(e - V(x))}$ represents the momentum of the particle moving along the x axis with energy e. The integration limits x_1 and x_2 are given by the classical turning points satisfying $p(x_i;e) = 0$. Semiclassical periodic-orbit theory (POT) based on the Feynman's path integral formalism has been developed since 1960s. Gutzwiller derived the famous *trace formula* [3] in which the quantum level density (density of states) is expressed in terms of the classical periodic orbits (POs). This formula gives a deep understanding on the origin of quantum fluctuations. Even the individual quantum states in non-integrable systems can be approximately constructed from classical dynamics by the use of the trace formula, but here attention will be focused on its important aspects in applications to the gross shell and supershell structures.

In section 2, semiclassical theories for the single-particle level densities and for the fluctuations in energies of many-body systems are briefly outlined. We will discuss the role of the classical POs, especially on the importance of the PO bifurcations and their relation to the restorations of local dynamical symmetries. In section 3, the radial power-law potential model and its scaling property are presented. In section 4, we apply the semiclassical POT to the spherical power-law potential model with spin-orbit coupling and study the origin of the nuclear magic numbers and that of the dynamical symmetry known as *pseudo-spin symmetry*. In section 5, the nuclear exotic deformations (superdeformations and octupole deformations) and the roles of PO bifurcations are analyzed. In section 6, the origin of prolate-shape dominance in nuclear ground-state deformations is investigated taking the spin-orbit

coupling into account. Section 7 is devoted to conclusions and perspectives.

2. Semiclassical theory of shell structure

As one sees from the successes in the mean-field approaches to nuclear many-body problems, quantum fluctuations in physical quantities are originated mainly from the shell effect due to the quantized single-particle motions in the mean field potential. In this section, we first describe the Strutinsky shell correction method to extract *shell energy*, the fluctuation part of the energy for many-body systems, from the single-particle spectrum. It will be shown that the shell energy is expressed in terms of the oscillating part of the single-particle level density. Next, we give a brief introduction to the semiclassical formula for the level density and shell energy, whose oscillating part is expressed as the sum over contribution of the classical POs. We will emphasize the importance of PO bifurcations for the enhancement of shell effect.

2.1. Shell correction method

In the independent particle picture for an interacting many fermion system, the constituent particle motion is quantized with the self-consistent mean-field Hamiltonian. Particles are arranged to the quantized states according to the Fermi statistics so that they minimize the total energy. Due to the interaction, total energy of the system considerably differs from a simple sum of the single-particle energies

$$E_{\rm sp}(N) = \sum_{j=1}^{N} e_j. \tag{2}$$

However, the oscillating part or $E_{\rm sp}$ is found to successfully describe the energy fluctuation of the total many-particle system. Strutinsky has derived the way with which one can unambiguously decompose $E_{\rm sp}$ into the average and oscillating parts [4,5] as

$$E_{\rm sp}(N) = \bar{E}_{\rm sp}(N) + \delta E(N). \tag{3}$$

By employing the realistic mean field model and replacing the average part $\bar{E}_{\rm sp}$ with more reliable semi-empirical formula, e.g. the liquid drop model (LDM),

$$E(N) = E_{\rm LDM}(N) + \delta E(N), \tag{4}$$

one can systematically describe the observed nuclear binding energies in good precisions.

To calculate the oscillating part δE from the single-particle spectra e_j, one first decompose the single-particle level density

$$g(e) = \sum_j \delta(e - e_j) \tag{5}$$

into the average and oscillating parts

$$g(e) = \bar{g}(e) + \delta g(e). \tag{6}$$

The average part is obtained by convolving the total one with a smoothing function f, for which a normalized gaussian of width γ with appropriate order of curvature corrections is usually employed:

$$\bar{g}_\gamma(e) = \frac{1}{\gamma}\int {\rm d}e' g(e') f\left(\frac{e-e'}{\gamma}\right), \tag{7a}$$

$$f(x) = \frac{1}{\sqrt{\pi}} {\rm e}^{-x^2} L_M^{(1/2)}(x^2). \tag{7b}$$

Here, the $2M$ th order curvature corrections are given by the Laguerre polynomial $L_M^{(1/2)}$, and we take $2M = 6$ in our numerical calculations. For a given γ, the *smoothed* Fermi energies $\bar{e}_F$ is defined thorough the particle-number condition

$$\int_{-\infty}^{\bar{e}_F(\gamma)} \bar{g}_\gamma(e){\rm d}e = N, \tag{8}$$

and the average part of (3) is obtained by

$$\bar{E}_{\rm sp}(N;\gamma) = \int_{-\infty}^{\bar{e}_F(\gamma)} e\bar{g}_\gamma(e){\rm d}e. \tag{9}$$

The smoothing width γ is determined so that $\bar{E}_{\rm sp}$ satisfies the so-called *plateau condition*

$$\frac{\partial}{\partial\gamma}\bar{E}_{\rm sp}(N;\gamma) \approx 0, \tag{10}$$

in order that the obtained $\bar{E}_{\rm sp}(N)$ is less dependent on the physically meaningless parameter γ. Inserting $g(e) = \bar{g}(e) + \delta g(e)$ into the particle-number condition for the exact Fermi energy e_F, one has the relation

$$\begin{aligned} 0 &= \int_{-\infty}^{e_F} g(e){\rm d}e - N \\ &= \int_{-\infty}^{e_F} \{\bar{g}(e) + \delta g(e)\}{\rm d}e - \int_{-\infty}^{\bar{e}_F} \bar{g}(e){\rm d}e \\ &= \int_{-\infty}^{e_F} \delta g(e){\rm d}e + \int_{\bar{e}_F}^{e_F} \bar{g}(e){\rm d}e \end{aligned} \tag{11}$$

Shell energy δE is then represented in terms of δg as

$$\begin{aligned} \delta E &= \int_{-\infty}^{e_F} e\ \{\bar{g}(e) + \delta g(e)\}\,{\rm d}e - \int_{-\infty}^{\bar{e}_F} e\bar{g}(e){\rm d}e \\ &= \int_{-\infty}^{e_F} e\delta g(e){\rm d}e + \int_{\bar{e}_F}^{e_F} e\bar{g}(e){\rm d}e \\ &\approx \int_{-\infty}^{e_F} (e - e_F)\delta g(e){\rm d}e. \end{aligned} \tag{12}$$

In the last step, the first e in the integrand of the second term is replaced with e_F, assuming $e_F - \bar{e}_F$ to be sufficiently small, and then the relation (11) is used. The last expression (12) for the shell energy will be used in the derivation of its semiclassical formula in the next subsection.

2.2. Level density in semiclassical approximation

In the small $\hbar$ limit, the quantum wave equation reduces to the classical equation of motion. Inserting the wave function of the form $\psi(\boldsymbol{r}, t) = {\rm e}^{{\rm i}F(\boldsymbol{r},t)/\hbar}$ into the Schrödinger equation ${\rm i}\hbar\partial\psi/\partial t = \hat{H}\psi(\boldsymbol{r}, t)$ and expand F in powers of $\hbar$ as $F = F_0 + \hbar F_1 + \cdots$, one has the classical Hamilton-Jacobi equation for $F_0 = S$:

$$\frac{\partial S}{\partial t} + H_{\rm cl}(\boldsymbol{p} = \boldsymbol{\nabla} S, \boldsymbol{r}) = 0 \tag{13}$$

in the leading order of $\hbar$, where $H_{\rm cl}(\boldsymbol{p},\boldsymbol{r}) = \boldsymbol{p}^2/2m + V(\boldsymbol{r})$ is the classical Hamiltonian. In the next-to-leading order, putting $F_1(\boldsymbol{r},t) = \frac{1}{2i}\log\rho(\boldsymbol{r},t)$, one has the continuity equation for the probability density $\rho = |\psi|^2$:

$$\frac{\partial\rho}{\partial t} + \boldsymbol{\nabla}\cdot(\rho\boldsymbol{v}) = 0, \tag{14a}$$

$$\boldsymbol{v} = \frac{\boldsymbol{\nabla}S}{m} \tag{14b}$$

and one has a picture of fluid running according to the classical equations of motion. In this way, the quantum dynamics can be related to the classical dynamics in the semiclassical approximation. Especially, classical POs are shown to play the central role in the level density and shell energy [3,6,7]. In the following, we shall briefly outline how the semiclassical formulas for the level density and shell energy are derived from the Feynman's path integral representation for the quantum propagator, and discuss the important aspects of the formulas in analyzing gross shell structures.

Energy level density $g(e)$ is given by the trace of the retarded Green's function $G^+(\boldsymbol{r}'',\boldsymbol{r}',e)$ as

$$g(e) = \mathrm{Tr}\,\delta(e-\hat{H}) = -\frac{1}{\pi}\,\mathrm{Im}\int \mathrm{d}\boldsymbol{r}\, G^+(\boldsymbol{r},\boldsymbol{r},e), \tag{15}$$

$$G^+(\boldsymbol{r}'',\boldsymbol{r}',e) \equiv \langle\boldsymbol{r}''|\frac{1}{e+\mathrm{i}\eta-\hat{H}}|\boldsymbol{r}'\rangle, \tag{16}$$

where η is a positive infinitesimal number. The Green's function is given by the Laplace transform of the propagator K as

$$G^+(\boldsymbol{r}'',\boldsymbol{r}',e) = \frac{1}{\mathrm{i}\hbar}\int_0^\infty \mathrm{d}t\,\mathrm{e}^{\mathrm{i}(e+\mathrm{i}\eta)t/\hbar}K(\boldsymbol{r}'',\boldsymbol{r}',t), \tag{17}$$

$$K(\boldsymbol{r}'',\boldsymbol{r}',t) = \langle\boldsymbol{r}''|\mathrm{e}^{-\mathrm{i}\hat{H}t/\hbar}|\boldsymbol{r}'\rangle. \tag{18}$$

Connection between quantum and classical mechanics is derived from the path integral representation for the propagator

$$K(\boldsymbol{r}'',\boldsymbol{r}',t) = \int \mathcal{D}[\boldsymbol{r}(t)]\exp\left[\frac{\mathrm{i}}{\hbar}\int_0^t L(\dot{\boldsymbol{r}},\boldsymbol{r})\mathrm{d}t'\right], \tag{19}$$

where the integral is taken over arbitrary paths connecting initial point $\boldsymbol{r}'$ and final point $\boldsymbol{r}''$ in time t. $\mathcal{D}[\boldsymbol{r}(t)]$ is the integration measure associated with the path $\boldsymbol{r}(t)$, and L is the Lagrangian function. The semiclassical formula of the propagator valid for small $\hbar$ is obtained by carrying out the above path integral using the stationary phase method (SPM).

For an introduction to the basic concept of the SPM, let us consider a one-dimensional integral of the form

$$I = \int \mathrm{d}q\, A(q)\mathrm{e}^{\mathrm{i}S(q)/\hbar}, \tag{20}$$

with $A(q)$ and $S(q)$ being moderate functions of q. Since $\hbar$ is small, above integrand is a rapidly oscillating function of q and may have no noticeable contribution to the integral due to the strong cancellation. Such cancellation is avoided in vicinity of the stationary point q^* of the function $S(q)$ satisfying $S'(q^*) = 0$, and it makes a dominant contribution to the integral. In the standard SPM, $S(q)$ is expanded around the stationary point q^* up to a quadratic order, and the above integral is evaluated approximately as

$$\begin{aligned} I &\approx A(q^*)\int_{-\infty}^{\infty}\mathrm{d}q\,\exp\left[\frac{\mathrm{i}}{\hbar}\left\{S(q^*)+\tfrac{1}{2}S''(q^*)(q-q^*)^2\right\}\right] \\ &= A(q^*)\mathrm{e}^{\mathrm{i}S(q^*)/\hbar}\sqrt{\frac{2\pi\mathrm{i}\hbar}{S''(q^*)}}. \end{aligned} \tag{21}$$

In general, $S(q)$ has several stationary points and equation (21) will be expressed in the sum over terms associated with all those points. This approximation is good for an isolated stationary point. However, it becomes worse as the second derivative $S''(q^*)$ becomes smaller, and then one should consider some higher order expansions of the action $S(q)$ around q^*.

Since the phase in equation (19) is the action integral along the path, the stationary solutions are nothing but the classical trajectory satisfying Hamilton's variational principle. Then, the propagator is expressed as the sum over contributions of classical trajectories. A detailed and clear derivation of the semiclassical formula from the path integral representation is found e.g., in section 7 of [8]. The result is expressed as

$$K_{\rm cl}(\boldsymbol{r}'',\boldsymbol{r}',t) = \frac{1}{\sqrt{(2\pi\hbar)^3}}\sum_\alpha \sqrt{D_\alpha}\exp\left[\frac{\mathrm{i}}{\hbar}R_\alpha - \frac{\mathrm{i}\pi\nu_\alpha}{2}\right], \tag{22}$$

which is known as the Van-Vleck formula. The sum in the right-hand side is taken over classical trajectories α starting from $\boldsymbol{r}'$ and arriving at $\boldsymbol{r}''$ in time t. R_α represents the action integral along α,

$$R_\alpha = \int_0^t L(\boldsymbol{r}(t'),\dot{\boldsymbol{r}}(t'))\mathrm{d}t', \quad \boldsymbol{r}(0) = \boldsymbol{r}', \quad \boldsymbol{r}(t) = \boldsymbol{r}'' \tag{23}$$

and D_α is given by

$$D_\alpha = \det\left(-\frac{\partial^2 R_\alpha(\boldsymbol{r}'',\boldsymbol{r}',t)}{\partial\boldsymbol{r}''\partial\boldsymbol{r}'}\right) = \det\left(\frac{\partial\boldsymbol{r}''}{\partial\boldsymbol{p}'}\right)^{-1} \tag{24}$$

which is related to the stability of the trajectory with respect to the initial condition. ν_α counts the number of *conjugate points* along the trajectory α, where the semiclassical propagator encounters singularities in coordinate space. Such singularities can be avoided by the Fourier transformation from the coordinate to momentum space before it encounters the conjugate point and then inverse Fourier transformation into coordinate space again after passing through the point. This can be also coped with by the catastrophe theory [9]. In such procedure, one generally has the delay of phase by $\pi/2$, as in the case of one-dimensional WKB wave function at the classical turning point.

Using the above semiclassical propagator $K_{\rm cl}$ in the Green's function (17) and inserting it into equation (15), the level density is expressed in the form

$$g_{\rm cl}(e) = \int \mathrm{d}\boldsymbol{r}\sum_\alpha A_\alpha(\boldsymbol{r};e)\exp\left[\frac{\mathrm{i}}{\hbar}S_\alpha(\boldsymbol{r},\boldsymbol{r};e) - \frac{\mathrm{i}\pi}{2}\nu_\alpha\right], \tag{25}$$

where the sum is now taken over the closed orbits which start $\boldsymbol{r}$ with energy e and return to $\boldsymbol{r}$ again. S_α is the Legendré transform of the action integral R_α, whose independent variable is transformed from time t to energy $e = -\partial R_\alpha/\partial t$ as

$$\begin{aligned} S_\alpha(\boldsymbol{r}'',\boldsymbol{r}';e) &= et + R_\alpha(\boldsymbol{r}'',\boldsymbol{r}',t) \\ &= \int_0^t (H+L)\mathrm{d}t' = \int_{\boldsymbol{r}'}^{\boldsymbol{r}''}\boldsymbol{p}\cdot\mathrm{d}\boldsymbol{r}. \end{aligned} \tag{26}$$

For a while, we shall leave out the explicit form of the prefactor A_α for simplicity, just mentioning that it is related to the stability of the trajectory with respect to the initial condition. Finally, the trace integral over $\boldsymbol{r}$ is carried out with the use of the SPM. The stationary phase condition is expressed as

$$\frac{\partial S(\boldsymbol{r},\boldsymbol{r};e)}{\partial \boldsymbol{r}} = \left[\frac{\partial S(\boldsymbol{r}'',\boldsymbol{r}';e)}{\partial \boldsymbol{r}''} + \frac{\partial S(\boldsymbol{r}'',\boldsymbol{r}')}{\partial \boldsymbol{r}'}\right]_{\boldsymbol{r}''=\boldsymbol{r}'''=\boldsymbol{r}} = \boldsymbol{p}'' - \boldsymbol{p}' = 0. \tag{27}$$

Coincidence of initial and final momenta $\boldsymbol{p}'' = \boldsymbol{p}'$ implies the orbit to be periodic. Hence, the semiclassical level density is expressed in terms of POs as

$$g(e) = \bar{g}(e) + \sum_\beta A_\beta(e)\cos\left(\frac{1}{\hbar}S_\beta(e) - \frac{\pi}{2}\mu_\beta\right). \tag{28}$$

The first term $\bar{g}(e)$ represents the average level density which corresponds to the contribution of zero-length orbit. The second term gives the oscillating part of the level density. The sum is taken over all the POs (not only primitive ones but also their repetitions). $S_\beta(e) = \oint_\beta \boldsymbol{p}\cdot \mathrm{d}\boldsymbol{r}$ is the action integral along the orbit β, and μ_β is the so-called Maslov phase index related to the geometric properties of the orbit β.

The prefactor $A_\beta(e)$ is also expressed in terms of the classical characteristics of the orbit β, such as the stability, period and degeneracy. Since the action $S_\beta(e)$ is in general a monotonically increasing function of energy e, each contribution of the PO gives an oscillating function of e, whose successive minima appear in a distance given by

$$\Delta e = \frac{2\pi\hbar}{dS_\beta/de} = \frac{2\pi\hbar}{T_\beta}. \tag{29}$$

T_β represents the period of the orbit β. This implies that the shorter POs having smaller periods T_β contribute to the level density oscillations of larger energy scales (having larger Δe). Therefore, the gross shell structure is determined by some shortest POs [10, 11]. Longer POs contribute to a finer structure superimposed on the gross one. Since the contributions of the POs having different periods give the terms oscillating with different Δe, they will interfere and build a certain beating pattern. The supershell structures, the modulations in shell structures, can be understood as the result of such interference effect. Balian and Bloch [6] have found a remarkable beating pattern in the coarse-grained level density for spherical cavity model, and it is understood as the interference effect of the equilateral triangular and square PO contributions. Nishioka *et al* have employed the semiclassical trace formula to account for the supershell structures in metallic clusters [12]. They have applied the idea of Balian and Bloch to a more realistic Woods-Saxon (WS) type mean field model, and have shown that the supershell structures observed in metallic clusters are successfully understood as the interference effect of the triangular and square-type POs. This is considered as one of the greatest successes in physical applications of the POT.

Let us next derive the semiclassical expression for the shell energy $\delta E(N)$. Inserting the semiclassical level density

$$\delta g(e) = \sum_\beta A_\beta(e)\cos\left(\tfrac{1}{\hbar}S_\beta(e) - \tfrac{\pi}{2}\mu_\beta\right) \tag{30}$$

into equation (12) and evaluating the integral using the semiclassical approximation, one obtains [10, 11]

$$\begin{aligned}\delta E(N) &= \sum_\beta \int_{-\infty}^{e_F} \mathrm{d}e(e-e_F)A_\beta(e)\cos\left(\tfrac{1}{\hbar}S_\beta(e) - \tfrac{\pi}{2}\mu_\beta\right)\\ &\approx \sum_\beta A_\beta(e_F)\int_{-\infty}^{e_F}\mathrm{d}e(e-e_F)\,\cos\Big[\tfrac{1}{\hbar}\big\{S_\beta(e_F)\\ &\qquad + T_\beta(e_F)(e-e_F)\big\} - \tfrac{\pi}{2}\mu_\beta\Big]\\ &= \sum_\beta \left(\tfrac{\hbar}{T_\beta(e_F)}\right)^2 A_\beta(e_F)\cos\left(\tfrac{1}{\hbar}S_\beta(e_F) - \tfrac{\pi}{2}\mu_\beta\right).\end{aligned} \tag{31}$$

From the first to second line in (31), the fact is used that the integrand in vicinity of the end point $e \approx e_F$ makes the chief contribution to the integral because the integrand is a rapidly oscillating function of energy due to the smallness of $\hbar$ and strong offsetting effect arises a little deep inside the integration region. Owing to the additional factor $(\hbar/T_\beta)^2$ in the last expression in equation (31), the contribution of longer POs are relatively suppressed, compared to the trace formula for the level density, and one usually needs only a small number of the shortest POs for the study of shell energies.

2.3. Periodic-orbit bifurcation and local dynamical symmetry

There are several different ways of deriving PO expansion formula depending on the integrability of the system. For a fully integrable (multiply-periodic) system, it is convenient to use the action-angle variables $\{\boldsymbol{I},\boldsymbol{\varphi}\}$, where the action variables $\boldsymbol{I}$ are constants of motion and the Hamiltonian is independent of the angle variables $\boldsymbol{\varphi}$. In an f-dimensional multiply-periodic system, generic classical trajectory is confined on a *torus*, an f-dimensional hypersurface in the phase space formed for given values of $\boldsymbol{I}$ with varying $\boldsymbol{\varphi}$. In such a system, energy is quantized according to the EBK (Einstein-Brillouin-Keller) torus quantization rule [7]

$$e_{\{n_k\}} = H(I_k = \hbar(n_k + \tfrac{1}{4}\alpha_k)), \quad (n_k = 0, 1, 2, \cdots) \tag{32}$$

which is a generalization of the one-dimensional Bohr-Sommerfeld quantization rule (1) to multi-dimensional integrable systems. Here, I_k is taken as the action integral along the k th irreducible loop Γ_k on the torus (which cannot be reduced to a point by any continuous deformation), and α_k is the so-called Maslov index which counts the caustic points encountered along Γ_k. Based on this quantization rule, Berry and Tabor derived a formula for the level density expressed as the sum over terms associated with the classical POs [13]. Creagh and Littlejohn have shown that the above Berry-Tabor formula can be also derived from the phase-space path integral representation of the quantum propagator [14]. For partially integrable systems, some of the trace integrals are carried out exactly, and they bring a factor proportional to the phase-space volume occupied by the PO family. Other integrals are carried out by the SPM, and they bring a factor related to the stability of the PO [14]. For a strongly chaotic system in which all the POs are isolated, one obtains the Gutzwiller trace formula [3, 7]

$$g(e) = \bar{g}(e) + \sum_\beta \frac{T_\beta^0(e)}{\pi\hbar\sqrt{|\det(M_\beta - I)|}}\cos\left(\frac{1}{\hbar}S_\beta(e) - \frac{\pi}{2}\mu_\beta\right). \tag{33}$$

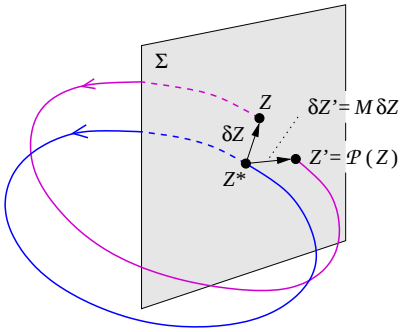


Figure 1. Illustration of the Poincaré map $\mathcal{P}(Z)$ defined by the phase plane Σ, and the monodromy matrix M associated with the PO Z^*.

Here, M_β represents the so-called monodromy matrix which describes the linearized stability of the PO, and T^0_β represents the period of the primitive PO β_0 in case β being its repetition. For a system with f degree of freedoms, let us consider a $(2f-2)$-dimensional phase plane Σ in the $(2f-1)$-dimensional energy surface. This phase plane defines a stroboscopic mapping known as *Poicaré map*: If the energy surface is compact, the trajectory starting at the point Z on the phase plane Σ will certainly intersect the same plane again, say, at point Z' with the same orientation as it started off (see figure 1). The map $\mathcal{P}:\Sigma\mapsto\Sigma$ which transforms Z into Z'

$$Z' = \mathcal{P}(Z) \tag{34}$$

according to the classical trajectory is called Poincaré map. PO Z^* is nothing but the fixed point of the Poincaré map

$$Z^* = \mathcal{P}(Z^*), \tag{35}$$

or more generally,

$$Z^* = \mathcal{P}^n(Z^*) \tag{36}$$

which returns to the initial point by the n th intersection.

The stability of the PO characterizes the behavior of adjacent trajectories with initial conditions infinitesimally shifted from Z^*. Expanding the Poincaré map around the PO Z^*, the monodromy matrix M is defined by the linear term as

$$Z^* + \delta Z' = \mathcal{P}(Z^* + \delta Z) = Z^* + M\delta Z + O(\delta Z^2), \tag{37a}$$

$$M_{ij} = \frac{\partial Z'_i}{\partial Z_j}. \tag{37b}$$

The factor $\det(M_\beta - I)$ in equation (33) originates from the trace integral in equation (15) carried out by the SPM, and this factor is proportional to the curvature of the action integral

$$C = \det\left(\frac{\partial^2 S}{\partial \boldsymbol{r}\partial \boldsymbol{r}}\right)_\perp . \tag{38}$$

The symbol $\perp$ indicates that the derivatives are taken with respect to the coordinates perpendicular to the PO, or to the manifold formed by the PO family under continuous symmetry. As mentioned above, the standard SPM breaks down if the curvature C vanishes. Let us show that a PO *bifurcation* is associated with this singularity.

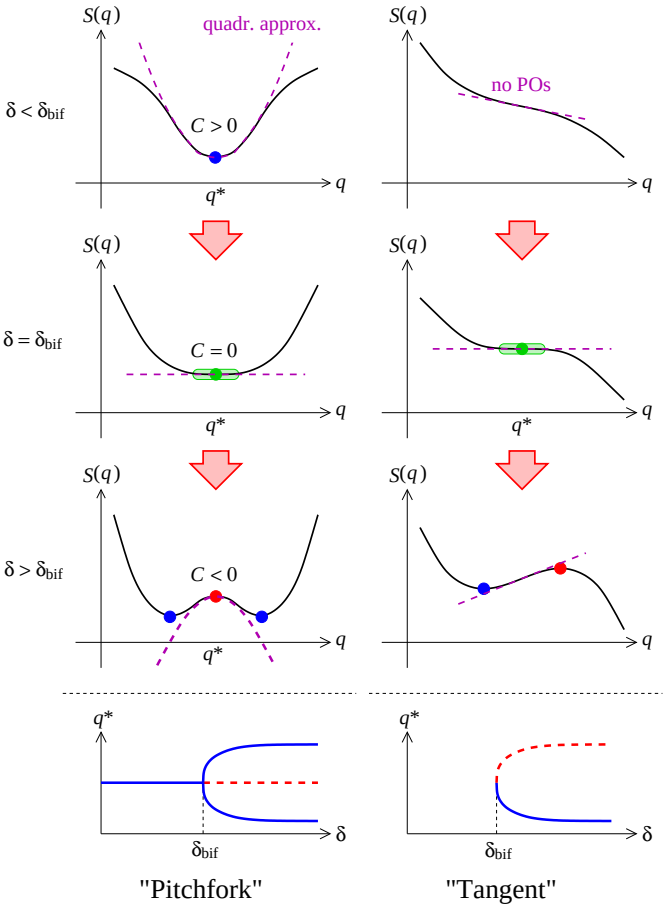


Figure 2. Illustration of PO bifurcation scenarios. Bifurcations proceed from the top to lower panels. POs correspond to the stationary points q^* of the action $S(q)$, and are indicated by dots. The number of POs changes when the parameter δ passes over the value $\delta_{\rm bif}$ where the curvature $C = S''(q^*)$ vanishes. The bifurcations shown in the left and right columns are called "pitchfork bifurcation" and "tangent bifurcation", respectively, named after the shapes of the graphs shown in the bottom panel, where the stationary points are plotted as functions of the parameter δ. The inverse processes (PO association or annihilation) are also called "bifurcation" in a broad sense.

Figure 2 illustrates two typical scenarios of the PO bifurcations. As wee see in equation (27), POs correspond to the stationary points of the action integral $S(q)$ along the closed orbit which start from q and returns to q again. Let us consider the situation in the top left panel in figure 2 where a single stationary point exists at q^* and the curvature C is positive there. One has the factor proportional to $1/\sqrt{C}$ by the integration with the SPM. With varying a parameter in the Hamiltonian, say, the deformation parameter δ, action $S(q)$ will continuously change and the curvature C may happen to vanish at $\delta = \delta_{\rm bif}$ as illustrated in the 2nd-row panel. After passing over this point, the sign of the curvature $C = S''(q^*)$ changes as illustrated in the 3rd-row panel, and one has new stationary points at both sides of the original one. This is a scenario of the PO bifurcation which is known as *pitchfork bifurcation*. Another type of bifurcation scenario called *tangent bifurcation* (or *saddle-node bifurcation*) is shown in the right column of figure 2, where a pair of stable and unstable POs are newly produced at the "bifurcation" deformation rather than emerging from already

existing one.[1] All the possible bifurcations in Hamiltonian systems are classified into six basic types by the catastrophe theory (see e.g. [15, 16]).

Due to the proportionality $\det(M_\beta - I) \propto C$, the monodromy matrix M has a unit eigenvalue if the curvature C vanishes. This unit eigenvalue suggests the formation of a local PO family around the bifurcating PO. If M has a unit eigenvalue, the associated eigenvector X_1 satisfies the relation

$$\mathcal{M}(Z^* + cX_1) \simeq Z^* + cMX_1 = Z^* + cX_1, \tag{39}$$

where c is a small continuous parameter. Hence, $Z^* + cX_1$ gives the continuous family of quasi-periodic family in vicinity of the PO Z^* as shown in the 2nd-row panels of figure 2. New PO(s) may emerge from this family. The PO bifurcation is thus associated with a vanishing curvature, or equivalently an emergence of unit eigenvalue in the monodromy matrix.

The formation of the above local PO family may indicate a local restoration of dynamical symmetry. In case where system has a continuous symmetry, each PO will form a continuous family generated by the symmetry transformation. Then, the PO bifurcation may imply that a dynamical symmetry is locally restored around the bifurcating PO and generates the above family of POs around it. To investigate which kind of invariance is acquired at the bifurcation point, let us consider the phase-space function

$$D(Z) \equiv \mathcal{P}(Z) - Z. \tag{40}$$

It represents the difference of successive intersections on the phase plane Σ by a classical trajectory, and is hence determined by the Hamiltonian flow. The PO Z^* is the zero of above function, namely, $D(Z^*) = 0$. If the monodromy matrix has a unit eigenvalue and the corresponding eigenvector is X_1, one has

$$\begin{aligned} D(Z^* + cX_1) &= \mathcal{P}(Z^* + cX_1) - (Z^* + cX_1) \\ &\simeq cMX_1 - cX_1 = 0 \end{aligned} \tag{41}$$

for small continuous parameter c. The local dynamical symmetry is thus expressed as the invariance of $D(Z)$ around Z^* with respect to the continuous transformation $Z = Z^* \to Z^* + cX_1$:

$$\left.\frac{\partial D}{\partial X_1}\right|_{Z^*} = 0. \tag{42}$$

The quasi-periodic family formed around the bifurcating PO is expected to make a coherent contribution to the path integral, and brings about a significant shell effect in case it is formed around a short PO. Such dynamical symmetry associated with PO bifurcation sometimes exerts significant effect on the level statistics [17].

To examine the effect of the bifurcation on the level density, it might be useful if the semiclassical formula valid also in the vicinity of bifurcation points is available. The effort of going beyond the standard SPM to cope with the bifurcation problem has been made in several approaches. In the uniform approximation [18], action function is expanded up to appropriate higher order terms. Those higher order terms have different function forms depending on the type of bifurcations, and one has to work out several kinds of catastrophe integrals to obtain formula valid around those bifurcation points. In another approach, the improved SPM [19, 20] is used in which the trace integration is carried out by expanding the phase up to a quadratic order but with keeping the exact finite integration limits. These approaches are applied to several integrable and non-integrable systems and succeeded in reproducing quantum mechanical results. In the following sections, we will show that the shell effects are considerably enhanced by the effect of the bifurcations of short POs, which play quite significant roles in characterizing various nuclear properties.

[1] Change in the number of solutions are generally called "bifurcation" in a wide sense.

3. The radial power-law potential model

The harmonic oscillator (HO) has been extensively used as a simple model of the mean-field for qualitative studies of nuclear structures. It nicely explains the low-energy single-particle spectra for light nuclei. It is also useful to understand the appearance of superdeformed shell structures. However, heavier nuclei have sharper potential surface and it is no longer described by the HO model. To consider the effect of the sharp surface, modified oscillator model is devised, in which a term $-v_{ll}\boldsymbol{l}^2$ ($\boldsymbol{l}$ being orbital angular momentum vector) is added to the HO potential. It describes the effect that the energies of the states with larger l, having major component around the surface, are relatively lowered by sharpening the potential surface. Taking also the spin-orbit coupling term $-v_{ls}\boldsymbol{l}\cdot\boldsymbol{s}$ into account, this model, known as the *Nilsson model*, is widely used as a convenient mean field which provides realistic single-particle levels for nuclei [1, 2, 21]. The square-well potential, which is further approximated by the infinite-well potential, is also used for a qualitative description of heavy nuclei. A realistic radial profile of the nuclear mean field potential is given by the WS model having a finite surface diffuseness. In this section, we propose a radial power-law potential $V(r) \propto r^\alpha$ which provides a good approximation to the WS potential and much easier to treat in both classical and quantum mechanics than the WS model. It includes HO and infinite-well models in its two limits $\alpha \to 2$ and $\alpha \to \infty$, respectively. We will discuss the scaling property of the power-law potential model which is extremely useful in the analysis of both classical and quantum dynamics.

3.1. The Hamiltonian and its scaling properties

The central part of the Woods-Saxon (WS) potential is written as

$$V_{\rm c}^{\rm WS}(\boldsymbol{r}) = -\frac{V_0}{1 + \exp[(r - R_A f(\Omega;\delta))/a]}, \tag{43}$$

where R_A and a represent the nuclear mean radius and the surface diffuseness, respectively. The shape function $f(\Omega;\delta)$ describes the angular profile of the nuclear-surface shape with angle variables $\Omega = (\theta,\varphi)$ of the spherical coordinate and the deformation parameter δ. For sufficiently stable nuclei, this potential can be approximated by a simpler power-law (PL) potential

$$V_{\rm c}^{\rm PL}(\boldsymbol{r}) = -V_0 + \frac{1}{2}V_0\left(\frac{r}{R_A f(\Omega;\delta)}\right)^\alpha \tag{44}$$

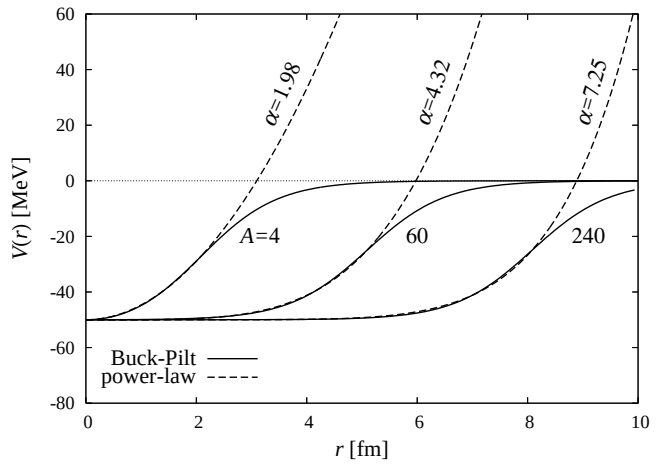


Figure 3. Radial profile of the radial power-law potential (broken line) fitted to the Buck-Pilt potential (full line) for several values of mass number A. Reproduced with permission from [24]. Copyright American Physical Society 2012.

with a suitable choice of the power parameter α. We determine the value of α by minimizing the volume integral of the squared difference of the two spherical potentials $V^{\rm PL}$ and $V^{\rm BP}$:

$$\frac{\mathrm{d}}{\mathrm{d}\alpha}\int_0^{R_A}\mathrm{d}r\, r^2\left[V_c^{\rm PL}(r;\alpha)-V^{\rm BP}(r)\right]^2=0, \tag{45}$$

$$V^{\rm BP}(r)=-V_0\frac{1+\cosh(R_A/a)}{\cosh(r/a)+\cosh(R_A/a)}. \tag{46}$$

Here, we use the Buck-Pilt (BP) potential $V^{\rm BP}$ [22, 23], which is essentially equivalent to the WS potential for surface diffuseness a sufficiently smaller than the radius R_A. The advantage of the BP in contrast with the WS is the absence of singularity at the origin, which is not critical at the present discussion but might be important for the analysis of classical POs intended in the future. Figure 3 displays the radial profile of the power-law potential fitted to the BP potential for several values of the mass number A. According to the universal WS parameter given in [25], we take the potential depth $V_0 = 50$ MeV, the radius $R_A = 1.3A^{1/3}$ fm and the surface diffuseness $a = 0.7$ fm. One obtains $\alpha = 4 \sim 7$ corresponding to the medium to heavy nuclei $A = 50 \sim 200$. Removing the constant term in equation (44), we define the model Hamiltonian as

$$H=\frac{p^2}{2m}+U_0\left(\frac{r}{R_0 f(\Omega;\delta)}\right)^{\alpha}. \tag{47}$$

Here, U_0 and R_0 are constants used as the units of energy and length, respectively, and m is the nucleon mass. Since the potential depends on U_0 and R_0 only in a form U_0/R_0^{α}, U_0 and R_0 are not necessarily independent and we put $U_0 = \hbar^2/mR_0^2$.

Our Hamiltonian (47) has the following scaling property

$$H(c^{1/2}\boldsymbol{p}, c^{1/\alpha}\boldsymbol{r}) = cH(\boldsymbol{p},\boldsymbol{r}), \tag{48}$$

regardless of deformation, and the classical equations of motion (EOM) are invariant under the scaling transformation

$$(\boldsymbol{r},\boldsymbol{p},t)\to(c^{1/\alpha}\boldsymbol{r}, c^{1/2}\boldsymbol{p}, c^{1/\alpha-1/2}t) \tag{49}$$

with energy $e \to ce$. This means that if $\boldsymbol{r}(t)$ is a solution of EOM at energy e, $c^{1/\alpha}\boldsymbol{r}(c^{1/\alpha-1/2}t)$ gives a solution of EOM at the energy ce. Therefore, one has the same set of POs at arbitrary energy, and the action integral along the orbit β is expressed in a simple function of energy as

$$S_\beta(e)=\oint_{\beta(e)}\boldsymbol{p}\cdot\mathrm{d}\boldsymbol{r}=\hbar\tau_\beta\mathcal{E}. \tag{50}$$

The last equation defines dimensionless variables which we call *scaled period* τ_β and *scaled energy* $\mathcal{E}$:

$$\tau_\beta\equiv\frac{1}{\hbar}\oint_{\beta(e=U_0)}\boldsymbol{p}\cdot\mathrm{d}\boldsymbol{r}, \tag{51a}$$

$$\mathcal{E}\equiv\left(\frac{e}{U_0}\right)^{1/2+1/\alpha}. \tag{51b}$$

The normal period T_β is related to τ_β by

$$T_\beta=\frac{\mathrm{d}S_\beta(e)}{\mathrm{d}e}=\hbar\tau_\beta\frac{\mathrm{d}\mathcal{E}}{\mathrm{d}e}. \tag{52}$$

Then, the Gutzwiller trace formula (33) for scaled-energy level density becomes

$$\begin{aligned} g(\mathcal{E}) &= g(e)\frac{\mathrm{d}e}{\mathrm{d}\mathcal{E}} \\ &\simeq \bar{g}(\mathcal{E})+\sum_\beta\frac{\tau_\beta}{\pi\sqrt{|\det(I-M_\beta)|}}\cos\left(\tau_\beta\mathcal{E}-\tfrac{\pi}{2}\mu_\beta\right). \end{aligned} \tag{53}$$

The average part $\bar{g}$ is given approximately by the Thomas-Fermi model $g_{\rm TF}$. For the power-law potential model, $g_{\rm TF}$ is obtained analytically by

$$g_{\rm TF}(e)=\int\frac{\mathrm{d}\boldsymbol{p}\mathrm{d}\boldsymbol{r}}{(2\pi\hbar)^3}\delta(e-H(\boldsymbol{r},\boldsymbol{p}))=\frac{1}{\pi\alpha}\,\mathrm{B}\left(\frac{3}{\alpha},\frac{3}{2}\right)\frac{\mathcal{E}^3}{e}, \tag{54}$$

where $\mathrm{B}(s,t)$ represents the Euler's beta function. This average density is independent of deformation under the volume conservation condition

$$\int\mathrm{d}\Omega f^3(\Omega;\delta)=4\pi. \tag{55}$$

Hence, the average part in equation (53) is given by

$$\bar{g}(\mathcal{E})\simeq g_{\rm TF}(e)\frac{\mathrm{d}e}{\mathrm{d}\mathcal{E}}=c_0\mathcal{E}^2, \tag{56a}$$

$$c_0=\frac{2\sqrt{2}}{\pi}\,\mathrm{B}\left(1+\frac{3}{\alpha},\frac{3}{2}\right). \tag{56b}$$

Under the existence of continuous symmetry, POs will be generally degenerate, namely, they form continuous family generated by the continuous symmetry transformations. In a spherical potential, generic PO forms a three-parameter family generated by the three independent rotations. As the exceptions, families of diameter and circle POs bear only two-parameter degeneracy since they are mapped onto themselves by one of the rotations. In an axially-symmetric potential, generic PO forms a one-parameter family generated by the rotation about the symmetry axis. The two exceptions are the diameter PO along the symmetry axis and the circle PO in the plane perpendicular to the symmetry axis. In a system with no

continuous symmetry, all the POs are isolated. In evaluating the trace integral with the SPM, one has the additional factor proportional to $1/\sqrt{S''} \propto \mathcal{E}^{-1/2}$. Each continuous symmetry avoids this factor and hence the contribution of K parameter family has the energy factor $\mathcal{E}^{K/2}$ relative to those for isolated POs. Taking account of this energy factor, semiclassical level density of the power-law potential model is generally expressed as

$$g(\mathcal{E}) = \bar{g}(\mathcal{E}) + \sum_{\beta} A_\beta \mathcal{E}^{K_\beta/2} \cos(\tau_\beta \mathcal{E} - \tfrac{\pi}{2}\mu_\beta), \tag{57}$$

with A_β independent of energy. In systems with continuous symmetries, there are POs having different degeneracies and K_β represents the degeneracy of the family β. The derivation of explicit forms of the amplitude factor under various continuous symmetries is found, e.g., in [10, 14].

3.2. Fourier transformation techniques

Due to the simple energy dependence of the action S_β in the power-law potential model, Fourier analysis of the quantum level density provides us a useful tool to investigate classical-quantum correspondence. Let us consider the Fourier transform of the level density with respect to scaled energy:

$$F(\tau) = \int \mathrm{d}\mathcal{E} g(\mathcal{E}) \mathrm{e}^{\mathrm{i}\tau\mathcal{E}} \mathrm{e}^{-(\gamma\mathcal{E})^2/2}. \tag{58}$$

The last Gaussian factor is introduced for the energy truncation. With quantum mechanically calculated eigenvalue spectrum $\{e_j\}$, scaled-energy level density is given by

$$g(\mathcal{E}) = \sum_j \delta(\mathcal{E} - \mathcal{E}_j), \quad \mathcal{E}_j = \left(\frac{e_j}{U_0}\right)^{1/2+1/\alpha}. \tag{59}$$

Inserting (59) into (58), one can evaluate $F(\tau)$ as

$$F^{\mathrm{qm}}(\tau) = \sum_j \mathrm{e}^{\mathrm{i}\tau\mathcal{E}_j} \mathrm{e}^{-(\gamma\mathcal{E}_j)^2/2}. \tag{60}$$

On the other hand, by inserting the semiclassical level density (57) into (58), ignoring the energy dependence of the amplitude for simplicity, one obtains the semiclassical expression

$$F^{\mathrm{cl}}(\tau) = \bar{F}(\tau) + \pi \sum_\beta A_\beta \mathrm{e}^{-\mathrm{i}\pi\mu_\beta/2} \delta_\gamma(\tau - \tau_\beta). \tag{61}$$

Here, $\delta_\gamma(x)$ represents the normalized Gaussian with width γ. Equation (61) tells that $F(\tau)$ is a function having successive peaks at the scaled periods of classical POs $\tau = \tau_\beta$ with the corresponding heights proportional to the amplitude A_β. Thus, one can extract information on the contribution of classical POs to the level density out of the quantum Fourier transform (60). The present method is very useful in examining classical-quantum correspondence, especially when the semiclassical amplitudes are difficult to obtain due to the hidden (exact or approximate) symmetries, bifurcations and so on. To obtain finer resolution (small γ) of POs in the Fourier spectrum, quantum spectra up to higher energy ($\mathcal{E} \sim 1/\gamma$) is required in evaluating (60).

Table 1. The values of the parameters α, R_0, $U_0 = \hbar^2/mR_0^2$ and κ in (63), obtained by fitting to the WS/BP model for several values of the mass number A.

A	α	R_0 [fm]	U_0 [MeV]	κ
20	2.80	2.32	3.32	0.089
100	5.23	3.93	1.14	0.059
200	6.75	5.06	0.72	0.049

3.3. Spin-orbit coupling

It is well known that the nuclear mean field potential has a strong spin-orbit coupling. In the WS model, the spin-orbit term

$$\frac{\lambda}{2(mc)^2}\left[\boldsymbol{\nabla}\frac{V_0}{1+\exp\{(r-R_A f(\Omega;\delta))/a\}}\right]\cdot(\boldsymbol{s}\times\boldsymbol{p}) \tag{62}$$

is added to the central potential. In the same manner as above, we introduce the spin-orbit term in our power-law potential model as

$$H = \frac{\boldsymbol{p}^2}{2m} + U_0\left(\frac{r}{R_0 f(\Omega;\delta)}\right)^\alpha + 2\kappa[\boldsymbol{\nabla}V_{\mathrm{so}}(\boldsymbol{r})]\cdot(\boldsymbol{s}\times\boldsymbol{p}), \tag{63}$$

with the spin-orbit potential

$$V_{\mathrm{so}}(\boldsymbol{r}) = \frac{1}{m}\left(\frac{r}{R_0 f(\Omega;\delta)}\right)^{\alpha_{\mathrm{so}}}. \tag{64}$$

Although the spin-orbit potential almost equivalent to the central one is used in the WS model, it might not be so bad to use the power parameter α_{so} a little different from α in the central potential (44). Here we choose $\alpha_{\mathrm{so}} = 1 + \alpha/2$ in order to keep the scaling relation

$$H(c^{1/2}\boldsymbol{p}, c^{1/\alpha}\boldsymbol{r}, \boldsymbol{s}) = cH(\boldsymbol{p}, \boldsymbol{r}, \boldsymbol{s}). \tag{65}$$

Apparently, this scaling is effective only for *frozen-spin* motions where spin vector is static. Fortunately, spin is frozen in many important POs, and the above scaling turns out to be very useful in our semiclassical analysis. The spin-orbit coupling strength κ is determined so that the spin-orbit potential in the spherical limit takes the same value as that of the realistic WS model at the nuclear surface $r = R_A$. The potential parameters obtained for several values of mass number A are shown in table 1. We obtain $\kappa = 0.05 \sim 0.06$ $\alpha = 5.0 \sim 6.0$ for medium-mass region $A = 50 \sim 150$.

The EOM for the classical spin variables are derived by the spin coherent-state path integral method [26]. One useful choice of the canonical variables for the spin degree of freedom is $q_s = \varphi$ and $p_s = s\cos\vartheta$, where ϑ and φ are polar and azimuthal angles in the spherical spin coordinates, respectively. The Cartesian spin components are given by

$$s_x = s\sin\vartheta\cos\varphi, \tag{66a}$$
$$s_y = s\sin\vartheta\sin\varphi, \tag{66b}$$
$$s_z = s\cos\vartheta, \tag{66c}$$

with the modulus s constant ($s = \hbar/2$ for nucleon). One can prove the Poisson bracket relation between the classical spin

variables

$$\{s_i, s_j\}_{\mathrm{P.B.}} = \frac{\partial s_i}{\partial q_s}\frac{\partial s_j}{\partial p_s} - \frac{\partial s_i}{\partial p_s}\frac{\partial s_j}{\partial q_s} = \epsilon_{ijk}s_k, \tag{67}$$

which exactly corresponds to the commutation relation of the quantum spin operators. The trace formula in extended phase space including the spin degree of freedom is formulated in [27].

Writing $\boldsymbol{B} = \boldsymbol{\nabla} V_{\mathrm{so}}(\boldsymbol{r}) \times \boldsymbol{p}$, classical EOM is expressed as

$$\dot{\boldsymbol{r}} = \frac{\partial H}{\partial \boldsymbol{p}} = \frac{\boldsymbol{p}}{m} - 2\kappa(\boldsymbol{s} \times \boldsymbol{\nabla} V_{\mathrm{so}}), \tag{68a}$$

$$\dot{\boldsymbol{p}} = -\frac{\partial H}{\partial \boldsymbol{r}} = -\boldsymbol{\nabla} V_c - 2\kappa \boldsymbol{\nabla}(\boldsymbol{B} \cdot \boldsymbol{s}), \tag{68b}$$

$$\dot{\boldsymbol{s}} = \{\boldsymbol{s}, H\}_{\mathrm{P.B.}} = -2\kappa \boldsymbol{B} \times \boldsymbol{s}. \tag{68c}$$

Let us consider the case where the potentials V (V_{c} and V_{so}) are axially symmetric. Frozen-spin orbits appear under the following conditions:

1. *Meridian and equatorial orbits*
   Taking z axis as the symmetry axis of rotation, consider a classical trajectory starting with $\boldsymbol{r}$ and $\boldsymbol{p}$ both on the meridian plane (the plane containing the symmetry axis), say, the (x, z) plane, and $\boldsymbol{s}$ perpendicular to it, namely, in the y direction. On the (x, z) plane, $\boldsymbol{\nabla} V$ is perpendicular to the y axis and then the vector $\boldsymbol{B}$ is parallel to the y axis. Consequently, the y-components of all the terms in the right-hand sides of equations (68a) and (68b) as well as the right-hand side of (68c) vanish, and the trajectory is shown to remain in the (x, z) plane with its spin frozen. Hence one has the meridian-plane frozen-spin orbits. If the potential is also symmetric with respect to the (x, y) plane (equatorial plane), the classical orbits in this plane with spin perpendicular to it are shown just as above to be frozen-spin orbits.

2. *Diameter orbits*
   Consider a trajectory starting along the symmetry axis (z axis) with spin parallel to the z axis. On the symmetry axis, $\boldsymbol{\nabla} V$ is parallel to the z axis and hence $\boldsymbol{B} = 0$. Thus one easily sees from the EOM (68) that the trajectory remains on the z axis with spin frozen, and one has the frozen-spin diameter PO along the symmetry axis. If the potential is symmetric with respect to the (x, y) plane, one finds just as above the frozen-spin diameter orbits in the equatorial plane with the spin parallel to the orbital motion.

The reduced EOM for the frozen-spin PO in the orbital plane have the same invariance against scaling transformation (48), and the action integral along the orbit is expressed as

$$\oint_{\beta(e)} \boldsymbol{p} \cdot \mathrm{d}\boldsymbol{r} = \hbar \tau_\beta \mathcal{E}. \tag{69}$$

Because of this simple energy dependence, equivalent to the case without spin-orbit coupling, contributions of those POs to the level density can be also studied conveniently with the Fourier transformation technique.

There is another semiclassical method to treat the spin degree of freedom, by making use of the coupled-channel WKB formalism [28–31], where the spin is considered as a slow variable in contrast to the orbital motion and the adiabatic approximation is applied. The Hamiltonian matrix of (2×2) spin channels is diagonalized to obtain two adiabatic Hamiltonians, and the classical POs in those two Hamiltonians determine the semiclassical level density. It should be noted that the frozen-spin POs in our approach are equivalent to those obtained for the *diabatic* representations of Hamiltonians in the coupled-channel WKB method [30].

4. Nuclear magic numbers and pseudospin symmetry

Nuclear binding energies as functions of the particle number show remarkable fluctuation properties similar to those in the ionization potentials of atoms. They are both manifestation of the shell structures for the quantized independent motion of constituent particles in the mean fields. In nuclear systems, quite distinct magic numbers are known for both protons and neutrons:

$$N, Z = 2, 8, 20, 28, 50, 82, 126, \cdots, \tag{70}$$

for which nuclei show the extreme stabilities. These numbers are successfully explained by the mean-field model with strong spin-orbit coupling, like Nilsson (modified oscillator) and WS potential models.

An approximate dynamical symmetry called pseudospin [or pseudo SU(3)] symmetry plays role in this shell structure [32–34]. In the so-called pseudospin transformation, angular momentum quantum numbers are reassigned as $\tilde{l} = l \pm 1$ for $j = l \pm \frac{1}{2}$ levels. The Nilsson Hamiltonian is transformed correspondingly as

$$\begin{aligned} &H_{\mathrm{Nils}} = H_{\mathrm{HO}} - v_{ls}\boldsymbol{l}\cdot\boldsymbol{s} - v_{ll}\boldsymbol{l}^2 \\ &\rightarrow\ \tilde{H}_{\mathrm{Nils}} = \tilde{H}_{\mathrm{HO}} - (4v_{ll} - v_{ls})\tilde{\boldsymbol{l}}\cdot\tilde{\boldsymbol{s}} - v_{ll}\tilde{\boldsymbol{l}}^2 - (2v_{ll} - v_{ls}). \end{aligned} \tag{71}$$

Since the relation $v_{ls} \approx 4v_{ll}$ holds well, spin-orbit coupling is quenched in the pseudospin representation, and one finds systematic degeneracies of the pseudo spin-orbit partners ($\tilde{j} = \tilde{l} \pm \frac{1}{2}$). The same kind of level degeneracies are also found in more realistic WS potential model, where the splittings of degenerate HO levels due to the sharp potential surface are partially compensated by the spin-orbit coupling. Those quenching of the pseudo spin-orbit splitting is considered as a result of approximate dynamical symmetry restoration, and might be understood in relation to the PO bifurcations as discussed in section 2.3.

In the power-law potential model, surface diffuseness is controlled by the power parameter α, and the above development of gross shell structure can be studied as the combinatory effect of the power parameter α and the spin-orbit coupling strength κ. Figure 4 shows the single-particle level diagram which plots single-particle scaled energies as functions of the spin-orbit parameter κ. The power parameter is taken as $\alpha = 5.0$ corresponding to the medium-mass nuclei. Systematic degeneracies of levels are found around the realistic value of spin-orbit strength $\kappa \approx 0.05$, where a gross shell effect is considerably developed. Level crossings of the pseudo spin-orbit partners are indicated by open dots. They occur at almost the same values of κ and affect the gross shell structure. The magic numbers (70) are correctly reproduced there.

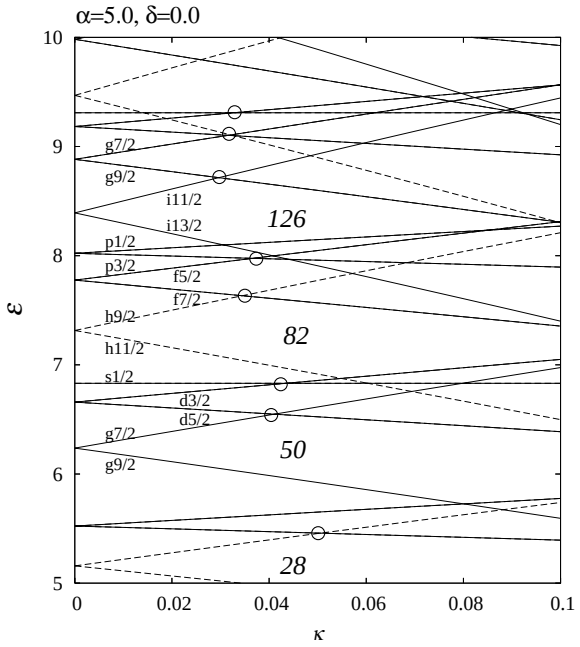


Figure 4. Single-particle level diagram for the spherical power-law potential model with the power parameter $\alpha = 5.0$. Scaled-energy levels $\mathcal{E}_j = (e_j/U_0)^{1/2+1/\alpha}$ are plotted as functions of the spin-orbit parameter κ. The particle numbers of the closed-shell configurations, where all the levels below the energy gap are occupied, are indicated in italics. Full and broken lines represent positive and negative parity levels, respectively. Open dots indicate the level crossings of the pseudo spin-orbit partners $\tilde{j} = \tilde{l} \pm 1/2$.

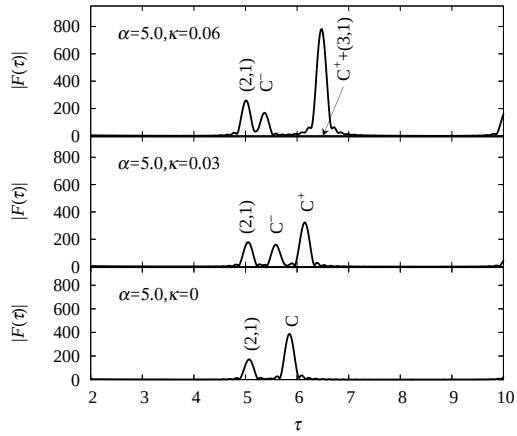


Figure 5. Quantum Fourier spectra $|F^{\rm qm}(\tau)|$ calculated for the power parameter $\alpha = 5.0$ with three different values of the spin-orbit parameter: $\kappa = 0$, 0.03 and 0.06.

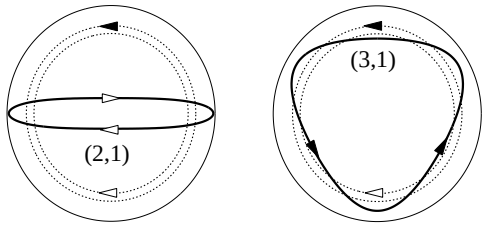


Figure 6. Some shortest classical POs in the spherical power-law potential model with spin-orbit coupling. The power parameter $\alpha = 5.0$ and the spin-orbit parameter $\kappa = 0.06$ are taken. In each panel, the outermost circle represents the boundary of the classically accessible region, dashed lines represent the circle orbits $C^{\pm}$, and thick solid lines represent the planar orbits (n_r, n_ϕ). Spin is frozen in the direction perpendicular to the orbital plane.

As discussed in section 3.2, one can extract information on PO contributions from the Fourier transform of scaled-energy level density (60). Figure 5 shows the moduli of Fourier transform $|F(\tau;\kappa)|$ as functions of τ, for several values of the spin-orbit parameter κ. As expected from equation (61), the Fourier amplitude shows successive peaks at the scaled periods of classical POs $\tau = \tau_\beta$. For $\kappa = 0$, one finds peaks at $\tau = 5.1$ and 5.8, which correspond to the diameter orbit (2,1) and the circle orbit C, respectively. We label the POs by the number of oscillation n_r in radial direction and number of rotations n_φ about the origin, and express them as (n_r, n_φ). The number of radial oscillations cannot be assigned to the circle PO and we denote it as C. With increasing spin-orbit parameter κ, the diameter orbit (2,1) is deformed into an oval shape, and the circle orbit C bifurcates into C^+ and C^- having orbital angular momentum parallel and anti-parallel to the spin. At $\kappa \simeq 0.05$, the circle orbit C^+ undergoes bifurcation and a new orbit (3,1) of triangular-type shape emerges. These POs at $\kappa = 0.06$ are displayed in figure 6. As shown in the top panel of figure 5, the contribution of the orbits C^+ and (3,1) is strongly enhanced at $\kappa = 0.06$. This is considered as the PO bifurcation enhancement effect which we discussed in section 2.2. Consequently, the semiclassical origin of the development of remarkable shell structure at $\alpha = 5.0$ and $\kappa = 0.05$, corresponding to medium-mass nuclei, is shown to be related to the emergence of the orbit (3,1) bifurcated from C^+ and the associated local dynamical symmetry.

The contribution of unfrozen orbit cannot be investigated by the Fourier analysis because of the absence of the scaling, and one can only study it by directly evaluating the semiclassical

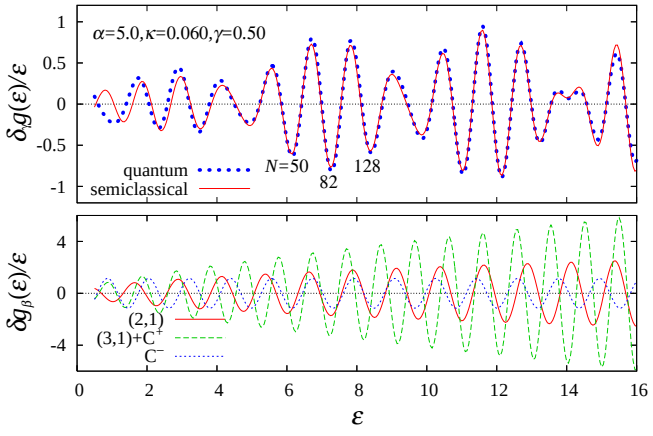


Figure 7. Oscillating part of the scaled-energy level density for the spherical power-law model with $\alpha = 5.0$ and $\kappa = 0.06$, coarse grained to a width $\gamma = 0.5$. The upper panel compares the quantum result and the semiclassical fit (72). The lower panel shows the contribution of individual POs in the semiclassical level density (73).

level density. If the quantum level density is reproduced only with the contribution of frozen-spin orbits, one may consider that the effect of unfrozen orbits can be omitted. Let us consider the oscillating part of the coarse-grained scaled-energy level density with the averaging width γ,

$$\delta_\gamma g(\mathcal{E}) = \frac{\gamma}{\sqrt{\pi}} \int \mathrm{d}\mathcal{E}' \delta g(\mathcal{E}') \mathrm{e}^{-\left(\frac{\mathcal{E}-\mathcal{E}'}{\gamma}\right)^2} = \sum_\beta \delta g_\beta(\mathcal{E})\, \mathrm{e}^{-(\gamma\tau_\beta)^2/4}, \tag{72}$$

$$\delta g_\beta(\mathcal{E}) \simeq A_\beta \mathcal{E}^{K_\beta/2} \cos(\tau_\beta \mathcal{E} - \tfrac{\pi}{2}\mu_\beta). \tag{73}$$

The exponential damping factor $\mathrm{e}^{-(\gamma\tau_\beta)^2/4}$ in (72), which appears due to the coarse-graining, suppresses the contribution of longer POs. Hence, the sum is dominated only by some shortest POs. We know the scaled periods τ_β and the degeneracies K_β, but unfortunately we have not succeeded in obtaining the semiclassical amplitudes A_β as well as Maslov indices μ_β. For the present, we shall treat A_β and μ_β as free parameters and determine them by the least square fitting to the quantum level density. Figure 7 shows the result for $\alpha = 5.0$ and $\kappa = 0.06$. We take account of the contributions of four shortest frozen-spin POs; (2,1), $\mathrm{C}^\pm$ and (3,1). In the upper panel, we compare the quantum level density with the semiclassical fitting. One will see that the quantum shell structure and its beating pattern are precisely reproduced. This seems to manifest that the PO sum is dominated mostly by the contribution of frozen-spin POs. In the lower panel, contributions of individual POs are shown, and one will see that the bifurcating orbits C^++(3,1) play the dominant role in this shell structure, as indicated in the Fourier spectra (figure 5). Interference with the contributions of the other POs makes the beating pattern. Particularly, one sees that the distinct magic numbers in the medium-mass region, $N = 50, 82, 128$, are established according to the constructive interference effect of those POs.

We have also found that the above (3, 1) bifurcation play significant roles in the quadrupole deformed shell structures. It might be an interesting subject to examine the role of the spin-orbit coupling for the properties of the deformed shell structures and their relations to the pseudo-spin symmetry in deformed nuclei [34–36].

5. Bifurcations of classical periodic orbits and nuclear exotic deformations

In the classical regime, self-bound interacting many-body system favors the spherical shape, since the system prefers the shape whose surface area is as smaller as possible under the fixed volume. In the quantum regime, the quantum shell effects evoke various deformations to the system. These shell effects are caused by the fluctuation in the single-particle spectra. Nuclei show particular stability at the spherical shape when the levels under the energy gap are completely occupied. The magic numbers (70) correspond to such closed-shell configurations. In situation where the degenerate levels at the Fermi energy are partially occupied, system tends to deform in order to lower the energy by splitting the degenerate levels by deformation, as illustrated in figure 8. The way of the level splittings depends on the types of the deformations, and such shape that makes the level density at the Fermi energy lower is preferred.

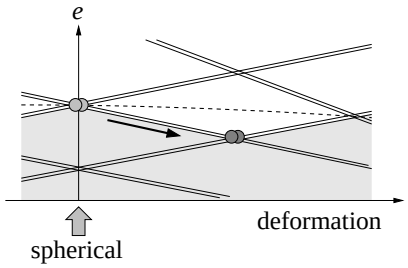


Figure 8. Illustration of the mechanism of deformation induced by the spontaneous symmetry breaking. Solid lines represent single-particle levels and dots denote particles in the highest partially-occupied levels. Broken line indicate Fermi energy. The self-bound system prefers the shape which makes level density at Fermi surface as low as possible to make the largest shell energy gain.

It is a kind of spontaneous breaking of symmetry similar to the Jahn-Teller effect known in the molecular systems. In this section, we discuss some nuclear exotic deformations and their semiclassical origins with the use of the POT.

5.1. Superdeformations

Concerning nuclear deformations, one of the most exciting discovery is the so-called *superdeformed states* in rapidly rotating nuclei, having extremely large quadrupole deformation whose axis ratio amounts to 2:1 [37, 38]. Nuclei with such large deformations are also found in the fission process as isomers formed between the double-humped potential barriers [39, 40]. The search of the second minima having much larger deformation whose axis ratio close to 3:1, often referred to as *hyperdeformed states*, is also a hot subject in the high-spin nuclear physics for both theories and experiments [41]. For such large deformations to be realized, significant shell energy gain should be provided particularly at those shapes in addition to the macroscopic driving force like Coulomb repulsion and rotation.

In the following, let us investigate the emergence of the superdeformed shell structures and their semiclassical origins. Here, we neglect the spin-orbit coupling for simplicity. The simplest model for describing the superdeformed shell structure is the axially-symmetric harmonic oscillator (HO)

$$H_{\mathrm{HO}} = \frac{\boldsymbol{p}^2}{2m} + \frac{m\{\omega_\perp^2(x^2+y^2) + \omega_z^2 z^2\}}{2} \tag{74}$$

with volume conservation condition $\omega_\perp^2 \omega_z = \omega_0^3$. Energy eigenvalues are given analytically by

$$e_{n_\perp n_z} = \hbar\omega_\perp(n_\perp + 1) + \hbar\omega_z(n_z + \tfrac{1}{2}), \tag{75}$$

and the simultaneous degeneracies of levels take places where the frequencies $\omega_\perp$ and ω_z become commensurable. Figure 9 displays the single-particle level diagram, in which the energy eigenvalues are plotted as functions of the deformation parameter $\delta = \log(\omega_\perp/\omega_z)$. Particularly, one sees prominent shell structures at $\mathrm{e}^\delta = 2^{\pm1}$ ($\delta = \pm 0.693$) and $\mathrm{e}^\delta = 3^{\pm1}$ ($\delta = \pm 1.099$), which correspond to the superdeformed and hyperdeformed shapes, respectively.

In semiclassical POT, those shell structures are understood as the result of the emergence of the four-parametric PO families

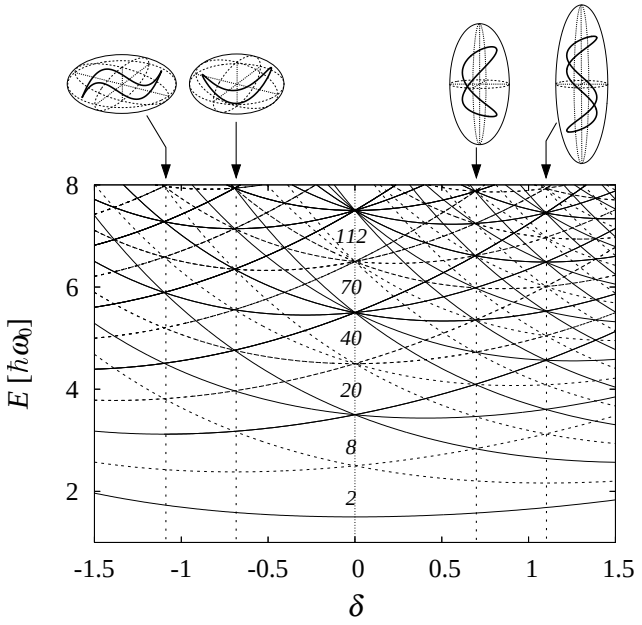


Figure 9. Single-particle level diagram for the axially deformed harmonic oscillator model. Energy eigenvalues are plotted as functions of deformation parameter δ. The particle numbers of the spherical closed-shell configurations, with the spin degeneracy factor taken into account, are indicated in italics. On the top of the diagram, typical classical POs at prolate and oblate super and hyper-deformed shapes are shown.

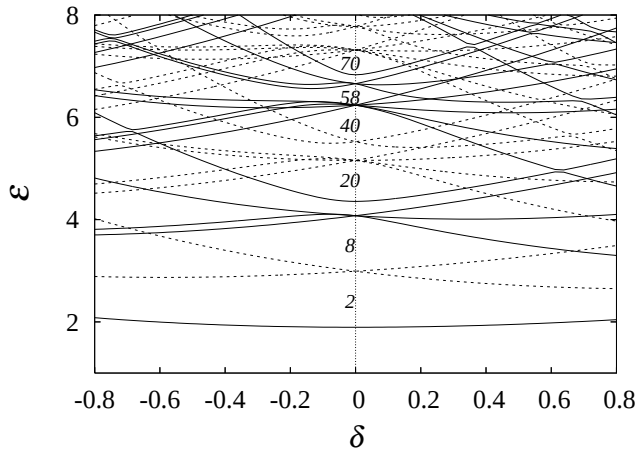


Figure 10. Single-particle level diagram for the spheroidal power-law potential model with the power parameter $\alpha = 5.0$. Scaled-energy levels $\mathcal{E}_j = (e_j/U_0)^{1/2+1/\alpha}$ are plotted as functions of the deformation parameter δ. The particle numbers of the closed-shell configurations at the spherical shape are indicated in italics.

at the deformations with rational frequency ratios. Typical POs at those deformations are shown in the top of figure 9. In the HO model, these degenerate PO families can exist only at the deformations with rational axis ratios.

On the other hand, realistic nuclear mean field potential has sharper surface with increasing mass number. Let us consider the deformed shell structure in the radial power-law potential model with spheroidal deformation, where the shape function

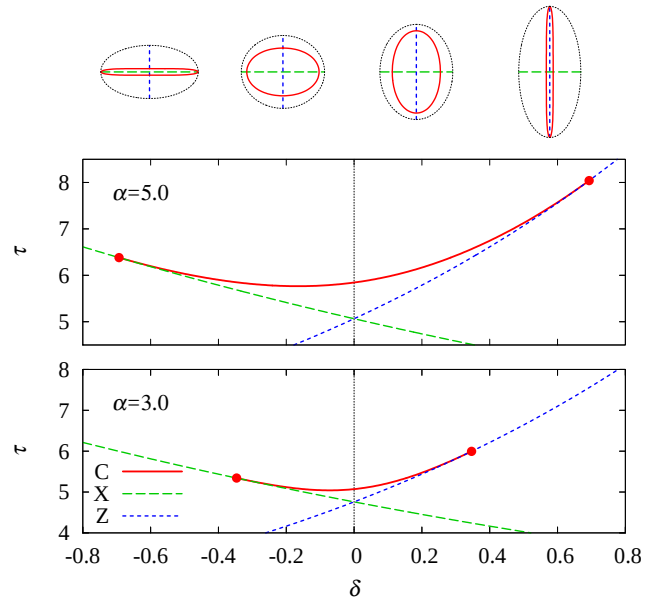


Figure 11. Scaled periods τ_β of the orbits C, X and Z plotted as functions of the spheroidal deformation parameter δ for the power parameter $\alpha = 3.0$ (lower panel) and 5.0 (upper panel). The orbit C makes a bridge between the orbits X and Z. Solid dots indicate the bifurcation points. Those three POs for $\alpha = 5.0$ at several values of δ are displayed on the top.

f in equation (47) is given by

$$f(\theta;\delta) = \frac{1}{\sqrt{\mathrm{e}^{-\frac{4}{3}\delta}\cos^2\theta + \mathrm{e}^{\frac{2}{3}\delta}\sin^2\theta}}. \tag{76}$$

This model is integrable in the two limits: $\alpha = 2$ (axially deformed HO) and $\alpha = \infty$ (spheroidal cavity), and nearly integrable between them: a large portion of the classical phase space is foliated with the KAM tori. Figure 10 shows the single-particle level diagram of the power-law potential model with the power parameter $\alpha = 5.0$. One finds level bunchings around the superdeformed region $|\delta| \sim 0.7$ although they are less clear compared with the case of HO.

Let us analyze the properties of classical POs in the spheroidal power-law potential to investigate the classical-quantum correspondence. In the HO limit, $\alpha = 2$, all the classical motions are periodic at the spherical shape ($\delta = 0$). Varying α from the HO value, only the circle and diameter POs survive. If the potential is deformed into spheroidal shape, the circle PO family bifurcate into the meridian oval family C and the isolated equatorial circle EC. The diameter PO also bifurcate into the degenerate equatorial diameter family X and the isolated symmetry-axis diameter Z. Figure 11 shows the scaled periods of those classical POs for several values of α as functions of the deformation parameter δ. With increasing prolate deformation $\delta > 0$, the meridian oval orbit C is continuously deformed and finally submerge into symmetry-axis diameter Z at certain deformation δ_c. With increasing oblate deformation $\delta < 0$, the orbit C is deformed in a different way and finally submerge into the equatorial diameter X at the deformation $-\delta_c$. In this way, the oval orbit family C make a bridge between the two bifurcations from the diameter orbits X and Z with varying deformation. We call such kind of bifurcation scenario as

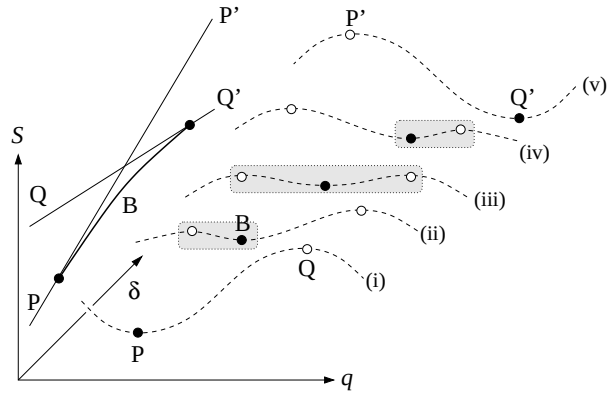


Figure 12. Illustration of the bridge-orbit bifurcation scenario. Broken lines represent $S(q)$, the action integral along the closed orbit starts from q and returns to the same point q, at several deformations in the bifurcation process. Stationary points of $S(q)$ give the POs. With varying deformation δ, a bridge orbit B emerges from the orbit P and then submerge into the orbit Q. A family of quasi-periodic orbits is formed around the shaded area. Full lines drawn in the (δ, S) plane are the action integrals along the POs, and dots indicate the bifurcation points. Reproduced with permission from [55]. Copyright American Physical Society 2014.

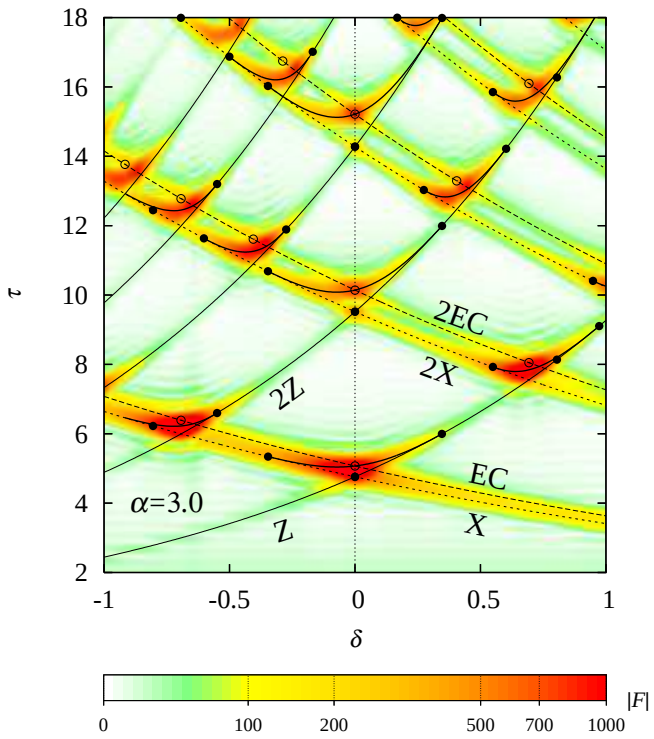


Figure 13. Color map of the quantum Fourier amplitude $|F^{\rm qm}(\tau;\delta)|$ in the (δ,τ) plane. The power parameter $\alpha = 3.0$ is taken. Lines represent the scaled periods $\tau_\beta(\delta)$ of some classical POs as functions of δ. Solid and open dots indicate the bifurcation points of the meridian orbits and equatorial orbits, respectively. EC, X and Z represent the equatorial circle, equatorial diameter and symmetry-axis orbits, respectively, and 2EC, 2X, 2Z are their second repetitions.

the *bridge orbit bifurcation*. The classical and semiclassical analyses of the bridge orbit bifurcations are given in [42] with various practical examples. It should be emphasized that the two orbits connected by the bridge are widely separated from each other in the phase space. If the bridge is short enough in the deformation space, the dynamical symmetry restored at one end of the bridge will be approximately kept along the bridge to the other end, and it may bring about a family of quasi-periodic orbits occupying much larger phase space volume than that in case of simple bifurcations.

Figure 12 illustrates the scenario of the bridge-orbit bifurcation:

(i) There are two different POs, P and Q, corresponding to the two stationary points of the action function $S(q)$, which are widely separated from each other.

(ii) With increasing deformation δ, the orbit P undergoes bifurcation and a new orbit B emerges from it. One finds a family of quasi-periodic orbits around these stationary points.

(iii) Action integrals of P and Q orbits crosses in the (δ, S) plane, and the quasi-periodic family extends from P to Q, implying a development of large dynamical symmetry around them.

(iv) The orbit B approaches the orbit Q and

(v) finally submerges into the orbit Q.

In comparison to the simple bifurcations which may cause local dynamical symmetries only in vicinity of the single bifurcating PO, we could expect the bridge orbit to give much more significant effect on the quantum shell effect due to the large phase-space volume of the quasi-periodic orbit family formed around the bridge orbits. From figure 11, one will note that existence domain $(-\delta_c, \delta_c)$ for the bridge orbit C grows as the power parameter α becomes larger. The contribution of bridge orbit might be less important as the above domain grows due to the breaking of the dynamical symmetry between the two ends of the bridge, and thus, shell effect is generally reduced as α increases.

To investigate the contribution of these orbits to the level density, we calculate the Fourier transforms of the scaled-energy level density (60). Figure 13 shows the Fourier amplitudes $|F(\tau;\delta)|$ plotted in the (δ,τ) plane. The power parameter $\alpha = 3.0$, a little larger than the HO value, is taken as an illustration. The scaled period $\tau_\beta(\delta)$ of the classical POs are also drawn in the same plane. One finds an excellent correspondence between Fourier peaks and the classical POs. The Fourier amplitudes take especially large values along the bridge orbits appearing at each crossings of the repetitions of the equatorial and symmetry axis orbits. One may also note that the Fourier amplitudes along the orbit nX (n th repetition of X) are larger than those along the orbit nZ. This is because the orbit X forms a one-parametric family with respect to the rotation about the symmetry axis, while the orbit Z is isolated. In the superdeformed region $\delta \approx 0.6$, the bridge orbits between the second repetition of equatorial orbits and the primitive symmetry-axis orbit play important role.

In figure 14, we examine the Fourier spectra in superdeformed region in detail taking the power parameter $\alpha = 5.0$ suitable for medium-mass nuclei. In the superdeformed region, the equatorial diameter X undergoes period-doubling bifurca-

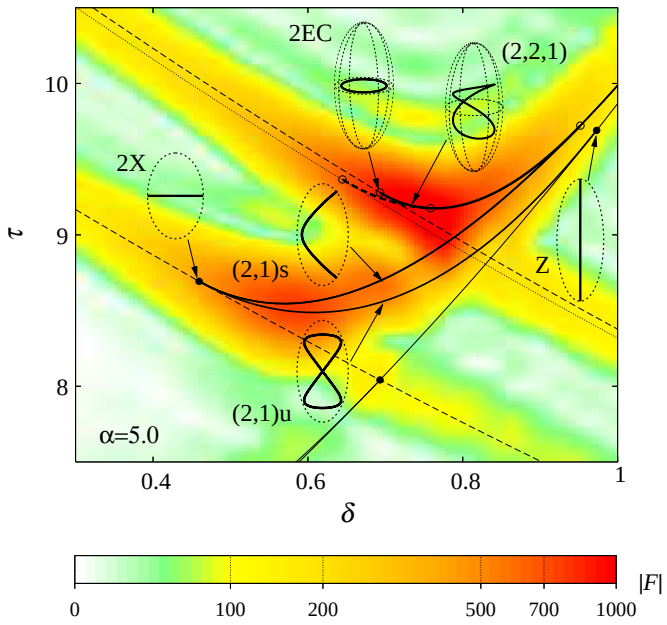


Figure 14. Color map of the quantum Fourier amplitude $|F^{\rm qm}(\tau,\delta)|$ for $\alpha = 5.0$ in the superdeformed region. Lines represent the scaled periods $\tau_\beta(\delta)$ of the classical POs as functions of δ, and dots indicate the bifurcation points. In each inserted figure, the PO is drawn with thick solid line, and the boundary of the classically accessible region is indicated by dotted ellipse(s).

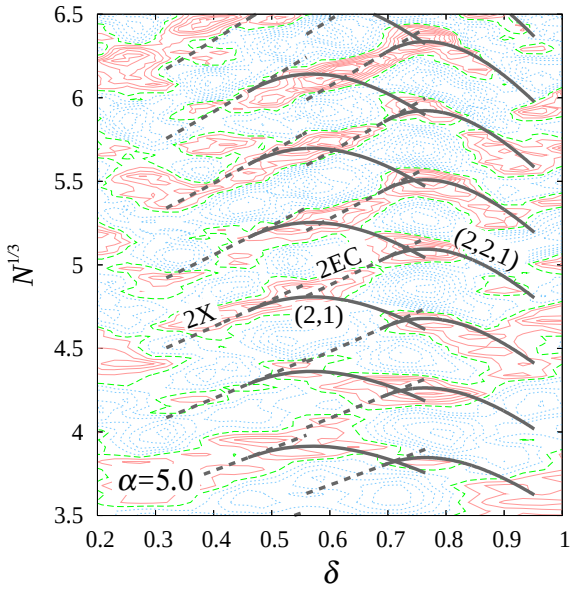


Figure 15. Contour map of the shell energy $\delta E(N;\delta)$ plotted in the $(\delta, N^{1/3})$ plane. Solid (red) and dashed (blue) contour lines represent negative and positive δE, respectively. Thick lines represent the constant-action ones (80) for some short classical POs in the portion where they make dominant contributions to the trace formula.

tion at $\delta = 0.46$ and a pair of stable and unstable meridian orbits (2,1)s and (2,1)u emerge. Here, the meridian orbits in the (x,z) plane are labeled by the numbers of oscillations in the x and z directions (n_x, n_z). The above meridian orbits change their shapes with increasing δ, and finally, (2,1)u submerge into the symmetry-axis orbit Z at $\delta = 0.97$, and (2,1)s submerge into Z at $\delta = 1.28$. Namely, there are two bridge orbits between equatorial diameter and symmetry-axis orbit. One also sees another bridge orbit between the second repetition of equatorial circle orbit 2EC and symmetry-axis orbit Z around a little larger deformation. The orbit EC undergoes period-doubling bifurcation at $\delta = 0.69$ and a new three-dimensional (3D) orbit (2,2,1) emerges. 3D orbits are labeled by the numbers of oscillations (rotations) (n_ρ, n_φ, n_z) in the directions of the cylindrical coordinate (ρ, φ, z). With increasing δ, the orbit (2,2,1) first submerge into meridian orbit (2,1)s (the stable branch of the meridian bridges) at $\delta = 0.95$ before finally submerge into the orbit Z at $\delta = 1.28$. One sees Fourier amplitude greatly enhanced along these bridge orbits and they should play most significant roles in emergence of superdeformed shell structure.

Next, let us evaluate the shell energies $\delta E(N)$ as functions of deformation, and examine the effect of above bifurcations. Suppose the situation where a single orbit β dominates the PO sum in equation (31), namely,

$$\delta E(N) \approx \left(\frac{\hbar}{T_\beta(e_F)}\right)^2 A_\beta(e_F)\cos\left(\frac{1}{\hbar}S_\beta(e_F) - \frac{\pi}{2}\mu_\beta\right). \qquad (77)$$

Then, the shell energy takes minima where the conditions

$$\tau_\beta(\delta)\mathcal{E}_F(N) - \frac{\pi}{2}\mu_\beta = (2n+1)\pi, \quad n = 0,1,2,\cdots \qquad (78)$$

are satisfied. Using the Thomas-Fermi approximation (56), Fermi energy $\mathcal{E}_F$ is approximately given as

$$N \approx \int_0^{\mathcal{E}_F} g_{\rm TF}(\mathcal{E})\mathrm{d}\mathcal{E} = \frac{c_0}{3}\mathcal{E}_F^3, \qquad (79a)$$

$$\mathcal{E}_F \approx \left(\frac{3N}{c_0}\right)^{1/3}. \qquad (79b)$$

Therefore, the shell energy will present valleys along the *constant-action lines* [11]

$$N^{1/3} = \left(\frac{c_0}{3}\right)^{1/3}\frac{(2n+1+\mu_\beta/2)\pi}{\tau_\beta(\delta)}, \quad n = 0,1,2,\cdots \qquad (80)$$

in the $(\delta, N^{1/3})$ plane. Figure 15 shows contour map of the shell energy $\delta E(N;\delta)$ in the $(\delta, N^{1/3})$ plane. One sees regular and strong oscillations in $\delta E(N)$ to develop around $\delta \approx 0.6$, which is considered as the effect of the superdeformed shell structure. Thick curves represent the constant-action lines (80) of some short classical POs. Shell energy valleys in the region $\delta = 0.4 \sim 0.6$ are nicely explained by the meridian (2,1) bridge orbits, and those in the region $\delta = 0.7 \sim 0.9$ are by the 3D orbit (2,2,1), just as expected from Fourier analysis. Hence, we can conclude that the bridge orbit bifurcations between the second repetition of equatorial and the primitive symmetry-axis orbits are responsible for the emergence of superdeformed shell structure. This is a general consequence valid for any value of α from HO to cavity values [43], any other parametrization of quadrupole shapes, with and without spin-orbit coupling [44].

5.2. Octupole deformations

The effect of reflection-asymmetric octupole degrees of freedom is also an important issue in nuclear structure physics [45].

Most of the nuclei are known to have reflection-symmetric ground states, and the violation of this fundamental symmetry may provide us with valuable information on the nuclear dynamics. As reviewed in [45], several static octupole-deformed states have been observed, e.g., through the low-lying negative parity states and the parity-doublet rotational bands connected with E1 and E3 transitions. It is also predicted that the excited rotational states have quite unique nature when they are build on the ground state having an octupole shape with the point group symmetry such as the tetrahedral one [46]. Since no driving forces towards reflection-asymmetric shapes are found in the classical dynamics, quantum shell effects are considered as the exclusive origin of the octupole deformations.

The reflection asymmetries are also important in description of the asymmetric fission processes of heavy elements [39, 47]. The semiclassical POT is also useful in accounting for the formation of fission path towards the reflection-asymmetric shapes [48].

Hamamoto *et al* have investigated the octupole deformed shell structures by considering four kinds of pure octupole deformations added to the spherical potential [49]. They found a remarkable shell structure develops at finite Y_{32}-type deformation which has the tetrahedral T_d symmetry. The importance of the tetrahedral deformation is also discussed for nuclei [50, 51] and metallic clusters [52]. Here we are going to extend the analysis of [49] to a more realistic power-law potential model and investigate the semiclassical origins of octupole-deformed shell structures. There are several ways of parametrizing octupole shapes. In the WS model, the shape of the equi-potential surface is usually parametrized as

$$r = R_0(1 + \beta_{3m}\tilde{Y}_{3m}), \tag{81a}$$

$$\tilde{Y}_{3m} = \sqrt{2 - \delta_{m0}}\,\mathrm{Re}\,Y_{3m}. \tag{81b}$$

In the modified oscillator model employed by [49], octupole potential is introduced in addition to the spherical central potential as

$$V(\boldsymbol{r}) = \frac{m\omega_0^2 r^2}{2}\left[1 - 2\beta_{3m}\tilde{Y}_{3m}\right]. \tag{82}$$

In this case, the shape of the equi-potential surface is expressed as

$$r = R_0[1 - 2\beta_{3m}\tilde{Y}_{3m}]^{-1/2}. \tag{83}$$

Above parametrizations can be generalized to a formula

$$r = R_0[1 + k\beta_{3m}\tilde{Y}_{3m}]^{1/k} \tag{84}$$

which corresponds to (81) for $k = 1$ and to (83) for $k = -2$, respectively. This generalized formula gives the identical shape independent of k up to the first order of β_{3m}, while it gives considerably different shapes dependent on k for large β_{3m}. To obtain the optimum shape parametrization, we consider minimization of the area of the equi-potential surface with respect to k under the fixed volume surrounded by the surface. For a given β_{3m} with varying k, the surface area is found to take minimum around $k = 0$. Hence we take the $k \to 0$ limit of equation (84), which results in an exponential function. Then, our Hamiltonian is expressed as

$$H = \frac{p^2}{2M} + U\left[\frac{r}{R_0(\beta_{3m})\exp(\beta_{3m}\tilde{Y}_{3m})}\right]^{\alpha}. \tag{85}$$

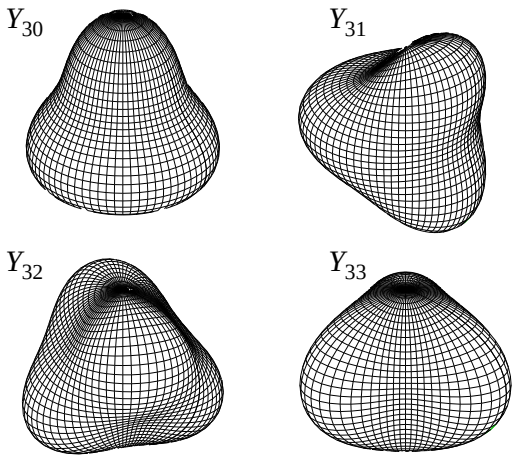


Figure 16. Equi-potential surfaces for octupole deformed potentials (85) for $\beta_{3m} = 0.4$.

$R_0(\beta_{3m})$ is determined by the volume conservation condition.

Figure 16 displays the equi-potential surfaces for four types of purely octupole-deformed potentials at the octupole parameters $\beta_{3m} = 0.4$. Y_{30} shape has a continuous axial symmetry, while the other shapes have different kinds of discrete point-group symmetries [53, 54]. Those symmetries can be utilized in quantum calculations to classify the eigenstates according to the irreps (irreducible representations) of the symmetry group. The Y_{31} and Y_{33} shapes have C_{2v} and D_{3h} symmetries, respectively, which have up to two-dimensional irreps. The Y_{32} shape has the tetrahedral (T_d) symmetry consists of 24 different symmetric transformations and has three-dimensional irreps. Since the degeneracy factor of the levels is equal to the dimension of the irrep, one generally find levels with three-fold degeneracies in the Y_{32}-deformed states. Due to this higher degeneracies, the Y_{32} deformed states are expected to have stronger shell effect than those with the other types of octupole shapes.

In addition to the above geometrical degeneracy effect, Hamamoto *et al* have found a strong bunching of levels for finite Y_{32} deformation, and the shell-energy gains with Y_{32} deformation may surpass those with quadrupole deformations in certain particle number regions.

Figure 17 shows the single-particle level diagram with the power parameter $\alpha = 6.0$, where the single-particle scaled energies $\mathcal{E}_j$ are plotted as functions of Y_{32}-deformation parameter β_{32}. The degenerate levels at the spherical shape split with increasing octupole deformation, but they eventually form a pronounced shell structure around $\beta_{32} = 0.4$. Surprisingly, the particle numbers corresponding to the closed-shell configurations are equivalent to those of spherical HO model [52]. Although the obtained shell effects here are not as strong as what we have obtained in [55] using the shape parametrization interpolating sphere and tetrahedron, qualitative features are quite similar. One finds no such remarkable shell structures for the other types of octupole shapes.

In figure 18, we compare deformed shell energies for different types of octupole shapes, taking the power parameter $\alpha = 6.0$. Shell energies $\delta E(N)$ are plotted as functions of the

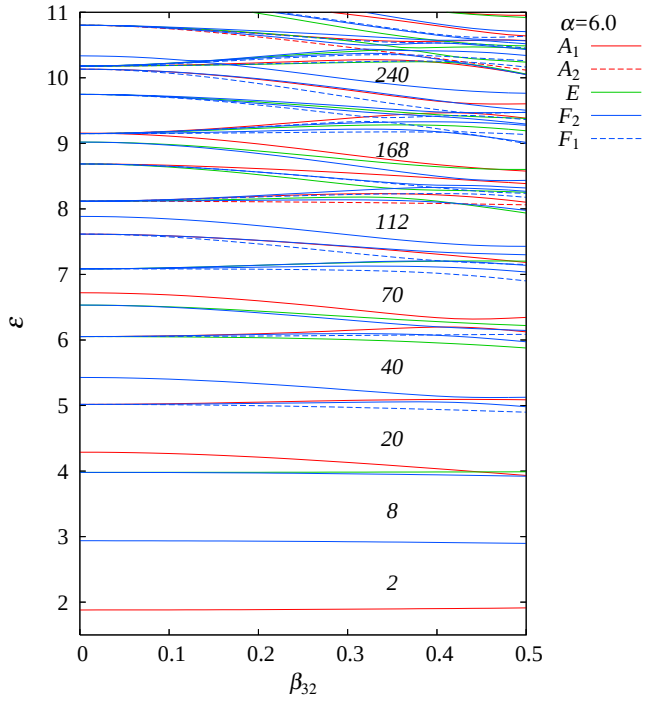


Figure 17. Single-particle level diagram of the octupole-deformed power-law potential model with the power parameter $\alpha = 6.0$. Scaled-energy eigenvalues are plotted as functions of Y_{32} deformation parameter β_{32}. Red solid and dashed lines represent the one-dimensional irreps A_1 and A_2, respectively, which have no degeneracies. Green solid lines represent the two-dimensional irrep E which are doubly degenerate. Blue solid and dashed lines represent the three-dimensional irreps F_2 and F_1, respectively, which are triply degenerate. The particle numbers of the closed-shell configurations around $\beta_{32} = 0.3 \sim 0.4$ are indicated in italics.

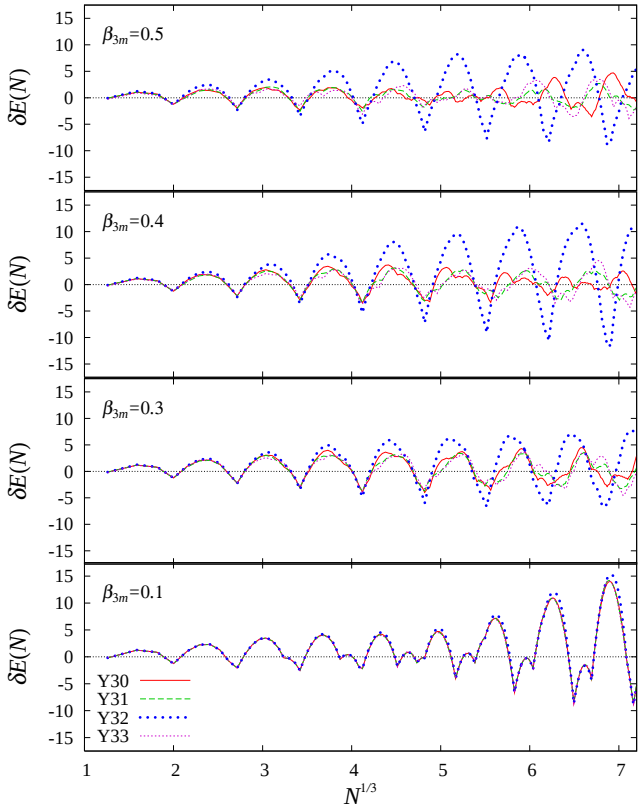


Figure 18. Shell energies as function of particle number N for several octupole parameters β_{3m} with the power parameter $\alpha = 6.0$. Red (solid), green (dashed), blue (thick dotted) and magenta (thin dotted) lines represent Y_{30}, Y_{31}, Y_{32} and Y_{33} deformations, respectively.

particle number N for several values of deformation parameters. For small β_{3m}, shell energies show supershell structures due to the interference of two groups of the POs: ones bifurcated from the circle orbit and the others from the diameter orbit. As the octupole deformation parameter increase, the fluctuations in shell energies show different structures and amplitudes for different types of deformation. One finds that the gross shell effects are remarkably enhanced for the Y_{32} deformation: It shows quite regular oscillations and are most developed around $\beta_{32} = 0.4$, as expected from the level diagram shown in figure 17.

Figure 19 shows the Fourier spectra $|F(\tau)|$ calculated for the octupole deformation parameters $\beta_{3m} = 0$, 0.2 and 0.4. For the spherical shape $\beta_{3m} = 0$, one sees two prominent peaks at $\tau = 5.15$ and 6.11 corresponding to the diameter and circle POs, respectively. These peaks rapidly decreases with increasing β_{3m} for $m \neq 2$, while the peak at $\tau \sim 6.0$ remains large for Y_{32} deformation. At $\beta_{32} \sim 0.4$, this peak is enhanced again and one might expect that the corresponding PO will make significant contribution to the level density at this deformation.

To elucidate the origin of the emergence of this remarkable shell structure associated with Y_{32} deformation, we examine in figure 20 the correspondence between the distribution of the Fourier peaks and the scaled-periods of the classical POs in the (β_{32}, τ) plane. Some shortest POs are displayed in figure 21

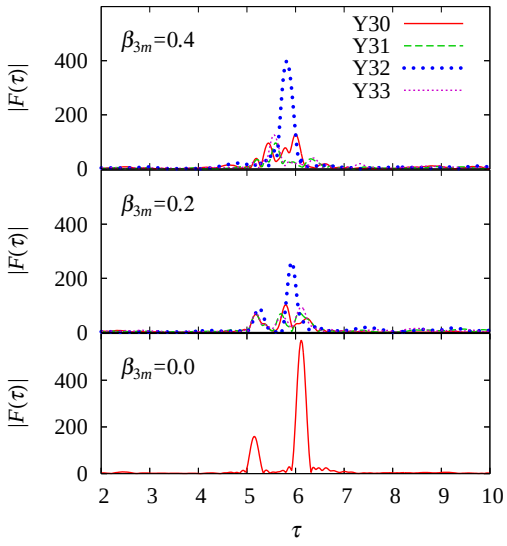


Figure 19. Quantum Fourier spectra $|F^{\rm qm}(\tau;\beta_{3m})|$ for the power-law potential models of spherical and various octupole shapes. The bottom, middle and top panels are for $\beta_{3m} = 0.0$ (spherical), 0.2 and 0.4, respectively. The results for the four different types of octupole shapes $\tilde{Y}_{30} \sim \tilde{Y}_{33}$ are plotted with red (solid), green (dashed), blue (thick dotted) and magenta (thin dotted) lines, respectively.

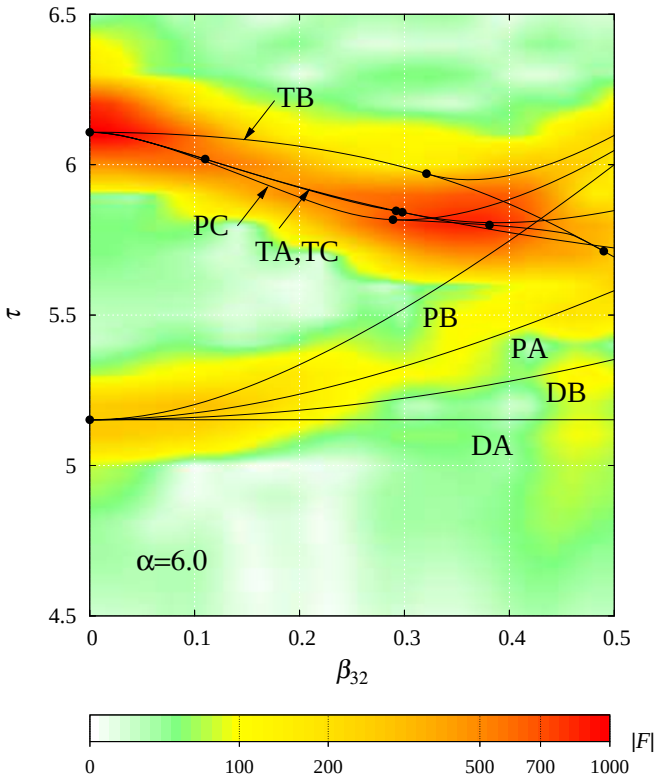


Figure 20. Color map of the quantum Fourier amplitude $|F^{\rm qm}(\tau;\beta_{32})|$ for $\alpha = 6.0$ plotted in the (β_{32},τ) plane. Curves represent scaled periods of the classical POs plotted as functions of octupole parameter β_{32}, and dots indicate their bifurcation points.

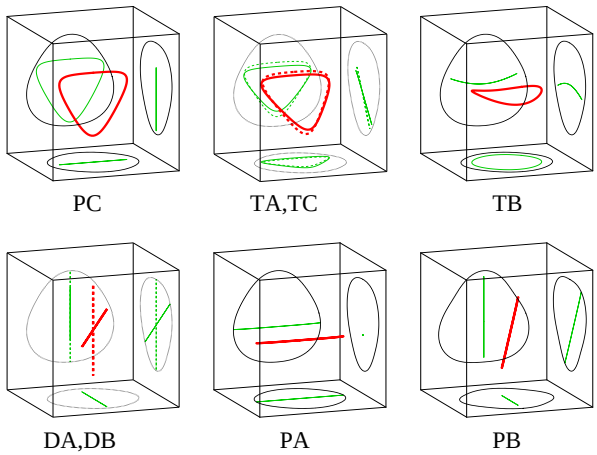


Figure 21. Some shortest classical periodic orbits for Y_{32} deformed state at the octupole parameter $\beta_{32} = 0.2$ with the power parameter $\alpha = 6.0$. Their projections onto the (x,y), (y,z) and (z,x) planes are also shown, with the boundaries of the classically accessible region.

for $\beta_{32} = 0.2$. Here, we name each PO with two characters: The first character "D", "P" or "T" stands for diameter, planar or three-dimensional; the second one is put alphabetically in the order we've found them. With increasing β_{32}, the diameter orbit bifurcates into four different orbits: the diameter DA along the three-fold rotation axis, the diameter DB along the four-fold rotatory reflection axis, librational orbits PA and PB in the mirror-symmetry plane. From the Fourier analysis, their contributions to the level density are monotonically reduced with increasing β_{32}. The circle orbit bifurcates into three orbits: the isosceles triangular-type orbit PC in the mirror plane, the equilateral triangular-type orbit TA having three-fold rotational symmetry, and the square-type orbit TB having four-fold rotatory reflection symmetry. The orbit PC undergoes bifurcation at $\beta_{32} = 0.035$ from which a 3D orbit TC emerges. The orbits TA and TC undergo so-called touch-and-go bifurcation at $\beta_{32} = 0.11$. As a common property in these three orbits, the monodromy matrix has an eigenvalue which is kept close to unity up to large values of β_{32}. As we discussed in section 2.3 a local family of quasi-periodic orbit is formed around such an orbit and it makes coherent contribution to the trace integral. This explains the reason why the contribution of these orbits remain large with increasing β_{32}. They undergo bifurcations almost simultaneously around $\beta_{32} \sim 0.3$ and yields new POs, some of which make bridges between them. As we see in figures 19 and 20, significant enhancement of the Fourier peak corresponding to those bifurcations is found. Some details on these bifurcations are described in the appendix. Since these orbits have almost the same values of scaled periods τ_β, they bring about a quite regular shell structure. The approximate coincidence of their actions and the almost simultaneous occurrence of bifurcations generating the bridge-orbit networks connecting them strongly suggest the underlying dynamical symmetry. This symmetry restoration, caused almost simultaneously around many different POs and also mapped onto their replicas generated by the 24 symmetry transformations of T_d, is considered to develop into in somewhat global one. Recalling the magic numbers at $\beta_{32} \approx 0.4$ shown in figure 17 which are equivalent to those of spherical HO, one may surmise that a restoration of the dynamical symmetry like SU(3) takes place for the above specific combination of surface diffuseness and tetrahedral-type octupole deformation. It raises an interesting question on the relation between the symmetry restoration and the tetrahedral deformation, and further studies are necessary to clarify it.

6. Nuclear prolate-shape dominance

Predominance of prolate shapes in nuclear ground-state deformation (which is referred to as *prolate dominance* for short) is a long-standing problem of nuclear structure physics [1]. Only a few oblate ground states are found experimentally in medium to heavy nuclei. The microscopic mean-field theories also support this feature [56]. In this section, we try to explain this peculiar property of nuclei from the semiclassical point of view with a realistic nuclear mean field model taking account of spin-orbit coupling.

6.1. Some earlier studies and remaining problems

Various approaches have been attempted aiming at a simple interpretation of the prolate dominance in nuclear ground-state deformations. It is generally recognized that the surface property of the mean-field potential has relevance to the deformed shell structures responsible for the prolate dominance. The surface of the mean field potential becomes sharper with increasing mass number. The transition of the deformed shell structure from light to heavy nuclei are studied by Strutinsky *et al* [11] using the WS potential model with spheroidal deformation. The deformation is parametrized by the axis ratio $\eta = R_z/R_\perp$ where R_z and $R_\perp (= R_x = R_y)$ are semiaxes of the nuclear surface. They calculated the shell energy $\delta E(N;\eta)$ as functions of deformation η and the particle number N, and investigated its ridge-valley structures in the (η, N) plane. For the prolate deformation ($\eta > 1$), the shell energy valleys have positive slopes in small N region while they turn into negative slopes in large N region. Such transition has been successfully explained using the POT. For small N, the surface diffuseness a is comparable with the nuclear radius R_A and the WS potential can be approximated by the anisotropic HO potential (74). Imposing the volume conservation condition $\omega_\perp^2\omega_z = \omega_0^3$, the oscillator frequencies are given as functions of axis ratio $\eta = \omega_\perp/\omega_z$ by

$$\omega_\perp = \omega_0\eta^{1/3}, \tag{86a}$$

$$\omega_z = \omega_0\eta^{-2/3}. \tag{86b}$$

In the normal deformation region, the two-parametric shortest equatorial orbit family makes the dominant contribution to the periodic-orbit sum. Its action integral is expressed as

$$S_\beta(E;\eta) = \frac{2\pi E}{\omega_\perp(\eta)} = \frac{2\pi E}{\omega_0\eta^{1/3}}. \tag{87}$$

Then, the constant-action lines (80) behave as

$$N(\propto E_F^3) \propto \eta \tag{88}$$

and they have positive slopes in the (η, N) plane. On the other hand, for large N, the surface diffuseness is much smaller than the nuclear radius and the WS potential looks more like a square-well potential, and it might be further approximated by the infinite-well (cavity) potential. In the spheroidal cavity, shortest equatorial orbits form a one-parametric family, while the meridian-plane orbits form a two-parametric family due to the specific symmetry of the system. Therefore, the meridian orbit families (triangular, quadrangular, ...) make dominant contributions to the PO sum. Imposing the volume conservation condition $R_\perp^2 R_z = R_0^3$, the semi-axes R_i of the equi-potential surface are given by

$$R_\perp (= R_x = R_y) = R_0\eta^{-1/3}, \tag{89a}$$

$$R_z = R_0\eta^{2/3}, \tag{89b}$$

and the length L_β of the meridian orbit, say, rhomboidal orbit is estimated as

$$L_\beta = 4\sqrt{R_\perp^2 + R_z^2} = 4R_0\eta^{-1/3}\sqrt{1+\eta^2}. \tag{90}$$

Then the action integral is expressed as

$$S_\beta(p) = pL_\beta \propto pR_0\eta^{-1/3}\sqrt{1+\eta^2} \tag{91}$$

and the constant action lines behave as

$$N(\propto p_F^3) \propto \frac{\eta}{(1+\eta^2)^{3/2}}, \tag{92}$$

which have negative slopes in the prolate region $\eta > 1$.

The semiclassical analysis of spheroidal cavity has been thoroughly worked out by Frisk [57] using the Berry-Tabor trace formula. The quantum mechanical shell energies are successfully reproduced by the semiclassical formula as the sum over PO contributions. He has remarked that the curves (92) in the oblate region $\eta < 1$ are rather flat, and correspondingly, the shell energy valleys running along them are also flat. Hence, no significant shell-energy gains are expected with oblate deformations as nucleon numbers deviated from the spherical magic numbers. This explains the mechanism of the prolate dominance very nicely.

Hamamoto and Mottelson [58] have discussed the origin of the prolate dominance from a different point of view. They compared the behaviors of the single-particle levels against deformation in the cases of the HO and cavity (infinite well) potential models. In axially deformed HO potential, the degenerate levels at the spherical shape fan out freely with increasing deformation on both prolate and oblate sides. This is because the shell oscillator number is a good quantum number in the HO model and interactions between levels from different major shells are absent. On the other hand, there are interactions between inter-shell levels in the cavity potential, and they affect the way of level fannings. Their behavior on the prolate and oblate sides show obvious asymmetry: the fannings of levels in the oblate side are considerably suppressed in comparison to the prolate side. Hamamoto and Mottelson have compared the effects of the interactions between inter-shell levels on the prolate and oblate sides, and clarified the reason why the level fannings show the above asymmetric behaviors on the prolate and oblate sides. The suppression of level fannings in the oblate side might reduce the chance to acquire a reasonable shell energy gain by oblate deformation. They considered the above asymmetry in level splittings as the origin of the prolate dominance.

Still there remain some questions to be answered. Firstly, from the semiclassical point of view, the deformations are essentially determined by the shell energy in which only short POs make contribution, and they are related to the gross shell structures. However, the way of level splittings might be related to rather fine structures of levels. One should consider this aspect more carefully. Secondly, as suggested by Tajima *et al* [59,60], prolate dominance shows strong correlation with the strength of spin-orbit coupling, as well as the surface diffuseness of the potential. The effect of spin-orbit coupling has not been studied in the above works. The argument of [58] applies to the case of realistic spin-orbit coupling where one finds the same kind of prolate-oblate asymmetry in the level fannings, but it cannot explain the *oscillation* in the prolate dominance with varying spin-orbit strength which Tajima *et al* have found. Let us consider these issues in the following part.

6.2. Gross shell structures in the power-law potential models

First, let us generalize the above analyses to a model having a more realistic radial dependence with finite diffuseness. Spin-orbit coupling is set aside for the moment. In [24], we have

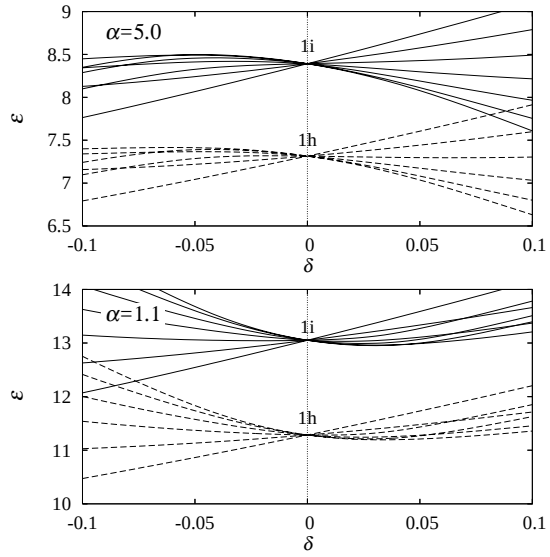


Figure 22. Splittings of the high-j single-particle levels with spheroidal deformation in power-law potential model for the power parameter $\alpha = 5.0$ and 1.1. Solid and dashed lines represent $1i$ and $1h$ levels, respectively. Reproduced with permission from [24]. Copyright Americal Physical Society 2012.

made analysis of the spherical and deformed shell structures for the power-law potential $V \propto r^\alpha$ with varying the power parameter α. For $\alpha = 2$, corresponding to the HO potential, level splitting occur in the same uniform way on both prolate and oblate sides. The shell energy valleys in the (δ, N) plain have almost the same upward-right slopes on both sides. With increasing α, the suppression of level fannings on the oblate side manifests. Figure 22 shows the level fannings of some high-j levels. In the upper panel for the power parameter $\alpha = 5.0$, corresponding to medium-mass nuclei, one clearly sees a remarkable suppression of level fannings on the oblate side. In the lower panel, a calculation for $\alpha = 1.1$ (although it is an unrealistic value for any nucleus) is made, in which one finds a suppression of level fannings on the prolate side, just as opposite to the case of $\alpha > 2$.

Figure 23 shows the contour maps of the shell energy $\delta E(N;\delta)$ plotted as a function of deformation δ and particle number N for the above two values of the power parameter α. Thick curves represent the constant action curves (80) of the POs which make dominant contribution to the trace formula (31). As we see in figure 11, the oval shape meridian-plane orbit family C exists as the bridge orbit between equatorial diameter orbit X and symmetry-axis diameter orbit Z. This bridge orbit makes significant contribution to the level density as expected from the Fourier spectra in figure 13. In the upper panel of figure 23 for $\alpha = 5.0$, one finds that the constant-action lines (80) for the orbit C nicely explain the shell energy valleys in the normal deformation region. The slopes of the curves are steep in the prolate side while they are rather flat in the oblate side. This behavior of the shell energy valleys formed along the bridge orbit C can be considered as the semiclassical origin of the prolate dominance. Thus, one sees that the argument of [57] for the spheroidal cavity model can be generalized to more realistic potentials.

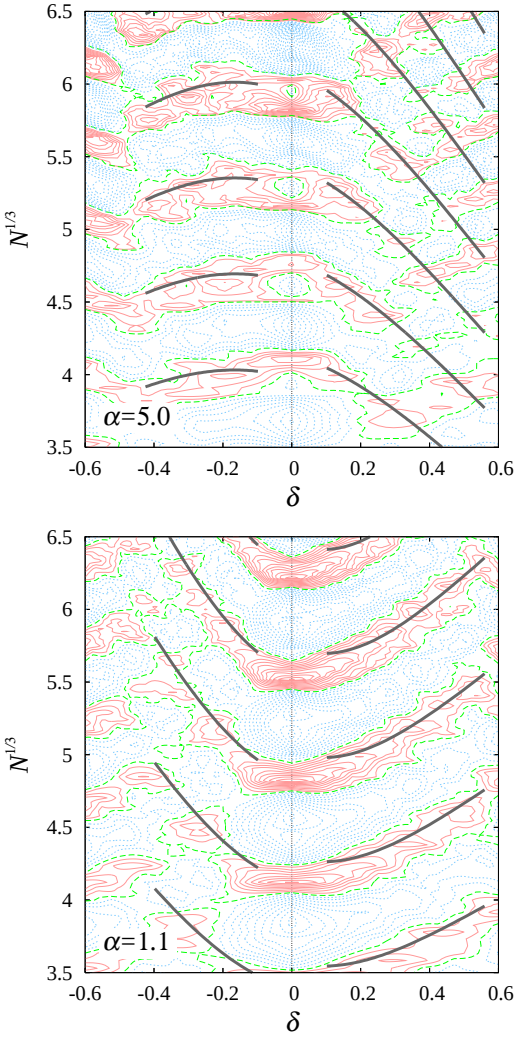


Figure 23. Contour map of the shell energy $\delta E(N;\delta)$ in the $(\delta, N^{1/3})$ plane for the spheroidal power-law potential model without spin-orbit coupling. Upper and lower panels are the results for the power parameter $\alpha = 5.0$ and 1.1, respectively. Solid (red) and dashed (blue) contour lines are drawn for negative and positive δE, respectively. Thick lines represent the constant-action ones (80) of the bridge orbit C.

To examine if the prolate shapes are really favored in energy due to the above behaviors of the deformed shell energies, we calculate the ground-state deformations $\delta_{\min}$ by minimizing the deformation energy

$$E_{\rm def}(N;\delta) = E(N;\delta) - E(N;\delta = 0) \tag{93}$$

with respect to the deformation parameter δ on each side of the oblate ($\delta < 0$) and prolate ($\delta > 0$) shape, and compare the energies at the prolate and oblate minima. In evaluating the total energy $E(N)$, sum of the single-particle energies $E_{\rm sp} = \sum_{i=1}^{N} e_i$ is employed in [58], but we shall make a little improvement [24]. Writing the mean-field Hamiltonian as $\hat{h} = \hat{t} + \hat{u}$ with $\hat{t}$ and $\hat{u}$ being the kinetic energy and the mean-field potential, respectively, average part of the total energy may be given by $\bar{E} \simeq \langle\hat{t}\rangle + \frac{1}{2}\langle\hat{u}\rangle$ if the mean field is a self-consistent one from a certain two-body interaction. Using $\bar{E}_{\rm sp} = \langle\hat{t}\rangle + \langle\hat{u}\rangle$ and the Virial theorem $\langle\hat{t}\rangle = \frac{1}{2}\langle \boldsymbol{r}\cdot\boldsymbol{\nabla}\hat{u}\rangle = \frac{\alpha}{2}\langle\hat{u}\rangle$ for the power-law model,

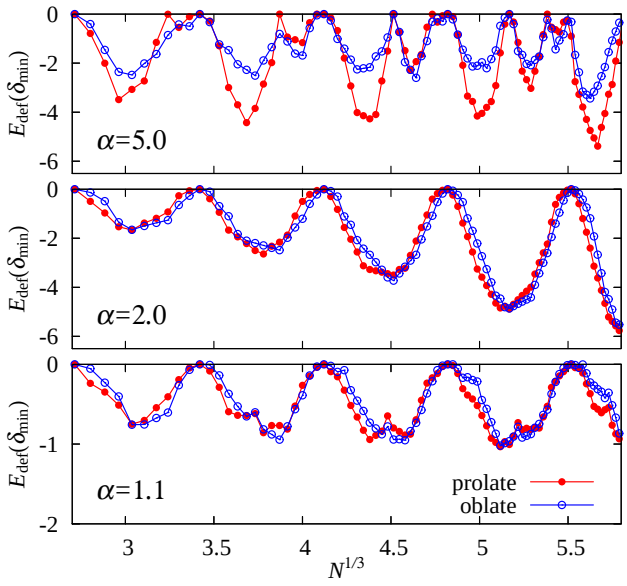


Figure 24. Comparison of the deformation energy minima (93) on the prolate ($\delta_{\rm min} > 0$) and the oblate ($\delta_{\rm min} < 0$) sides, plotted as functions of the cubic root of the particle number N. Bottom, middle and top panels show the results for the power parameter $\alpha = 1.1$, 2.0 and 5.0, respectively.

one has

$$\langle \hat{u} \rangle = \frac{2}{\alpha+2}\bar{E}_{\rm sp}, \tag{94a}$$

$$\langle \hat{t} \rangle = \frac{\alpha}{\alpha+2}\bar{E}_{\rm sp}, \tag{94b}$$

$$\bar{E} = \frac{\alpha+1}{\alpha+2}\bar{E}_{\rm sp}, \tag{94c}$$

and therefore

$$E(N) = \frac{\alpha+1}{\alpha+2}\bar{E}_{\rm sp}(N) + \delta E(N). \tag{95}$$

Figure 24 compares the deformation energy minima $E_{\rm def}(\delta_{\rm min})$ on the prolate and oblate sides for several values of the power parameter α. $\delta_{\rm min}$ is the deformation parameter where the deformation energy (93) takes minimum on each of the prolate and oblate side. For $\alpha = 2.0$ (HO), systems with single-particle orbits filled up to the lower half of the spherical shell prefer prolate shapes while those up to the upper half prefer oblate shapes, and the numbers of systems that have the lowest energies at prolate and oblate shapes are comparable. For $\alpha = 5.0$ where the potential surface is considerably sharper than HO, prolate minima turn systematically lower than oblate ones and they clearly show the prolate dominance. For $\alpha = 1.1$, where one sees the suppression of level fannings on the prolate side which may imply oblate-shape dominance, no essential difference between prolate and oblate minima are found in the deformation energies. Looking at the shell energy contour plot for $\alpha = 1.1$ shown in the lower panel of figure 23, one sees that the constant-action lines for the orbit C have considerably large slopes on the prolate side as well as on the oblate side. These constant-action lines nicely explain the behavior of the shell-energy valleys, for which no remarkable prolate-oblate asymmetry is expected.

To summarize above results, the prolate dominance is strongly correlated with the behavior of shell energy valleys, and its origin is clearly understood as the contribution of short classical POs. Correlation between the level fannings and the shape dominance is missing in the case of $\alpha = 1.1$. This might be because the level fannings are related to rather finer shell structure associated with the contribution of longer POs and their roles in the shell energies (31) are less important.

6.3. Effect of spin-orbit coupling

Next, let us consider the effect of spin-orbit coupling. By means of the systematic Strutinsky calculations over the whole nuclear chart, Tajima *et al* examined the occurrence of the prolate dominance by varying the surface diffuseness and spin-orbit strength of the mean-field potential [59, 60] in order to single out the parameter which is playing the essential role. They have calculated the ground state deformations of all the observed combinations of (N, Z) in nuclear chart to extract the ratio of the numbers of prolate and oblate ground states, and have examined its dependence on the strength of l^2 potential (surface diffuseness) and ls potential (spin-orbit strength) in the Nilsson (WS) model. As the results, they found a strong interference between the effects of surface diffuseness and spin-orbit strength on the prolate/oblate ratio. Particularly, the prolate dominance disappears when the spin-orbit parameter is reduced to the half of its realistic value. Considering this result, the analysis based on the model without taking account of spin-orbit coupling is giving us only partial understandings for the prolate-shape dominance of real nuclei. For a deeper understanding of this feature, we make a semiclassical analysis of the prolate-oblate asymmetry taking the spin-orbit coupling into account.

Figure 25 shows the level diagram for the power parameter $\alpha = 5.0$ and spin-orbit parameter $\kappa = 0.06$, which are considered as realistic for medium-mass nuclei. The spherical magic numbers (70) are correctly reproduced with those values of the parameters. The behaviors of the level splittings with increasing prolate and oblate sides look similar to the case without spin-orbit coupling: one sees the same suppression of level fannings on the oblate side as we see in the case without spin-orbit coupling (see the upper panel of figure 22). Hence it seems that the argument in [58] also applies to the case of finite spin-orbit coupling.

However, behavior of the deformed shell energies show quite strong dependence on the spin-orbit parameter. Figure 26 shows the contour maps of the shell energies $\delta E(N; \delta)$ as functions of the deformation parameter δ and the particle number N, for the power parameter $\alpha = 5.0$. We compare the results for the case of realistic value of the spin-orbit parameter $\kappa = 0.06$ and for the reduced value $\kappa = 0.03$ where Tajima *et al* found disappearance of the prolate dominance. One may notice the obvious difference in the valley structures in the deformed shell energies in those two maps, especially on the oblate side. For $\kappa = 0.06$ the valley lines on the oblate side are approximately flat, while for $\kappa = 0.03$, one finds valleys with considerably large slopes.

Figure 27 compares the prolate and oblate deformation-energy minima $E_{\rm def}(N; \delta_{\rm min})$ for different values of κ with fixed value of the power parameter $\alpha = 5.0$. The bottom panel for

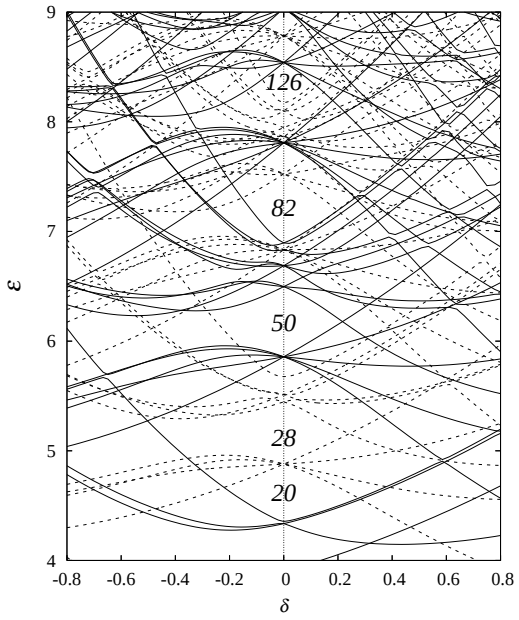


Figure 25. Single-particle level diagram for the power-law potential model with the power parameter $\alpha = 5.0$ and spin-orbit parameter $\kappa = 0.06$. Scaled-energy eigenvalues $\mathcal{E}_j = (e_j/U_0)^{1/\alpha+1/2}$ are plotted as functions of spheroidal deformation parameter δ. Solid and broken lines represent positive and negative parity levels, respectively. The particle numbers of the closed-shell configurations are indicated in italics.

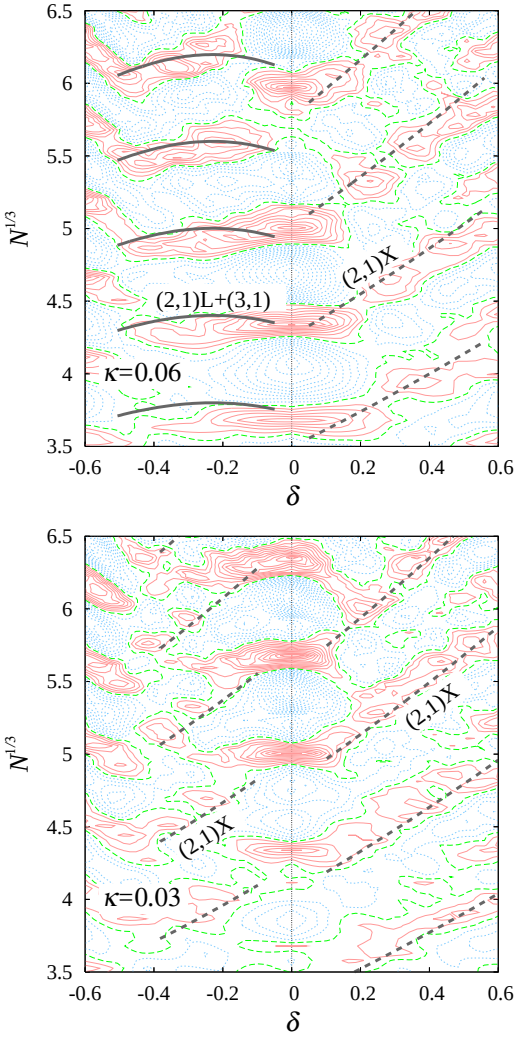


Figure 26. Contour map of the shell energy $\delta E(N;\delta)$ in the $(\delta, N^{1/3})$ plane. Solid (red) and dotted (blue) contour lines represent the negative and positive δE, respectively. Thick lines represent the constant-action ones (80) for some important short POs.

$\kappa = 0$ is equivalent to the top panel of figure 24. With increasing κ, the differences between prolate and oblate energy minima are reduced at $\kappa = 0.03$, the half of the realistic value, manifesting the disappearance of prolate-shape dominance. However, the differences grow again for the realistic value $\kappa = 0.06$ and the prolate minima become considerably lower than the oblate ones, implying the *revival* of the prolate-shape dominance. All these results nicely correspond to the behavior of shell energy valleys found in figure 26. Therefore, it is essential to describe the above behavior of the shell energy valleys with varying spin-orbit strength for understanding the origin of prolate dominance observed in real nuclei.

To understand the above changes in deformed shell structures from semiclassical view point, we investigated the effect of spin-orbit coupling on the properties of the classical POs. Figure 28 illustrates what kinds of changes are induced in the shortest POs when the spin-orbit coupling is switched on. For $\kappa = 0$, one has two diameter orbits X and Z, and the bridge orbits C connecting them at $\delta = \pm\delta_c$ as one sees in figure 11. With increasing spin-orbit strength κ, the periods of the orbits $C^{\pm}$, whose orbital angular momenta parallel and anti-parallel to the spin, separate from each other into L and S (denoting long and short, respectively). The changes in diameters X and Z show peculiar dependence on the deformation. The left part ($\delta < -\delta_c$) of X and the right part ($\delta > \delta_c$) of Z changes into oval orbit with orbital angular momenta parallel to the spin and are continuously connected with L at $\pm\delta_c$, while the right part ($\delta > -\delta_c$) of X and the left part ($\delta < \delta_c$) of Z changes into those having the opposite directions of orbital angular momenta and cause tangent bifurcations with S at $\delta = \pm\delta_c$. One should also note that, with increasing spin-orbit parameter κ, the bifurcation deformation δ_c becomes smaller and the orbit (2,1)S shrinks to a small deformation domain (see appendix for some detailed analyses on those bifurcations). On the other hand, the orbit (2,1)L survives for any larger deformation. With increasing κ, it undergoes bifurcation and new triangular-type orbits (3,1)X and (3,1)Z (which are symmetric with respect to the x and z axes, respectively) emerge from it at around $\kappa = 0.05 \sim 0.06$, depending on the deformation δ. Therefore, the orbits (2,1)L and (3,1)'s have almost the same values of scaled periods at $\kappa = 0.06$. Those orbits should make coherent contribution to the level density, and are expected to give significant effects on the deformed shell structures for wide range of deformation δ due to the bifurcation enhancement effect discussed in section 2.2.

Thanks to the scaling relation for those frozen-spin orbits, we can make use of the Fourier analysis in investigating how their contributions change with varying κ. Figure 29 shows the moduli of Fourier transforms $|F(\tau;\delta)|$ of the quantum scaled-energy level densities, calculated for $\kappa = 0.03$ and 0.06. Thick lines show the scaled periods of some shortest POs which are

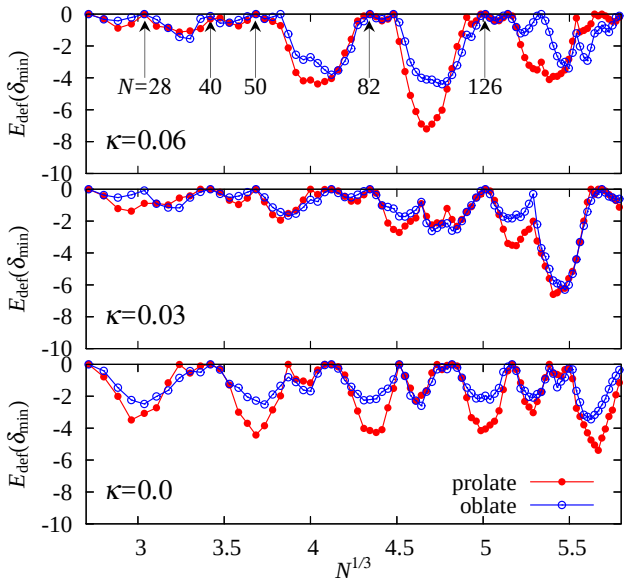


Figure 27. The same as figure 24 but for several values of the spin-orbit parameter κ with the fixed power parameter $\alpha = 5.0$. Bottom, middle and top panels show the results for $\kappa = 0.0$, 0.03 and 0.06, respectively.

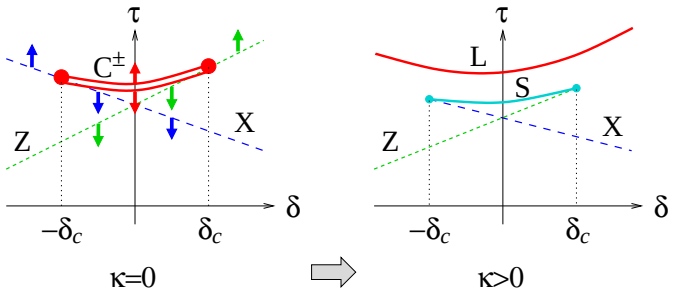


Figure 28. Illustration of the changes in the classical POs in the spheroidal power-law potential model induced by the spin-orbit coupling. The scaled periods τ of some shortest POs are shown as functions of the deformation parameter δ. Arrows in the left panel indicate the directions of the changes in τ with increasing spin-orbit strength κ.

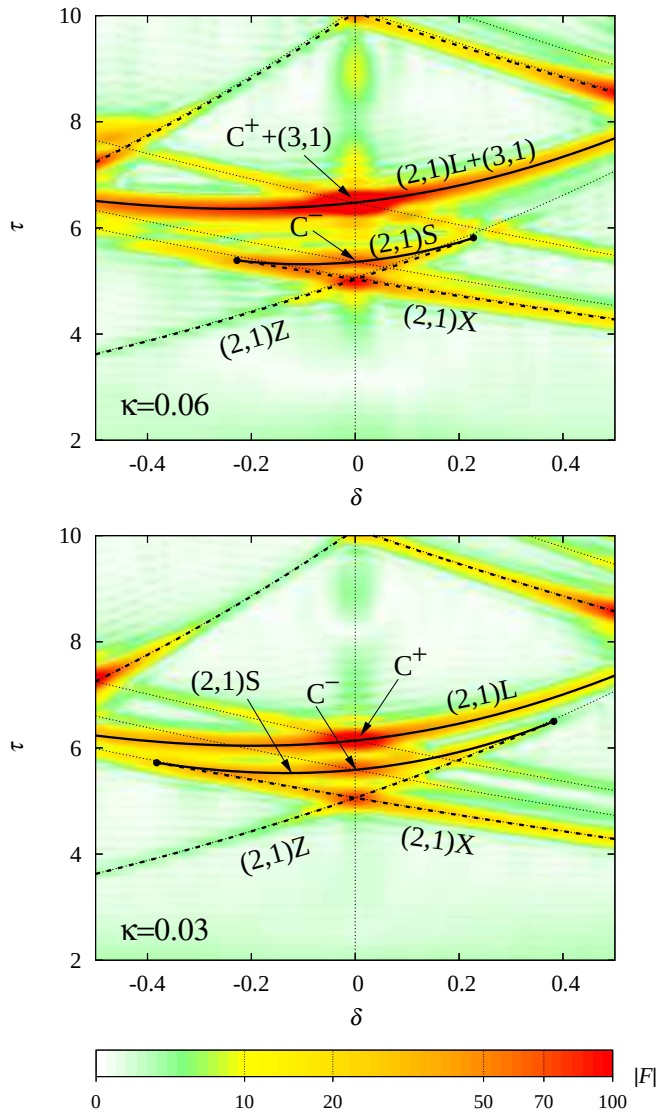


Figure 29. Color map of the quantum Fourier amplitude $|F^{\rm qm}(\tau;\delta)|$ in the (δ,τ) plane. The power parameter is $\alpha = 5.0$ and the spin-orbit parameter is $\kappa = 0.06$ and 0.03 for the upper and lower panels, respectively. Lines represent the scaled periods $\tau_\beta(\delta)$ of the classical POs, and the dots indicate the bifurcation points.

displayed in figure 30. One finds that the Fourier amplitudes have peaks exactly along these meridian frozen-spin POs. The cross sections along the vertical line at several deformations are shown in figure 31 in order to see the relative strengths of the Fourier amplitudes.

On the prolate side, one finds considerable Fourier peak at the shortest orbit (2,1)X, and it is expected to make major contribution to the shell energy. On the oblate side, the shortest orbit is (2,1)Z, but its contribution is smaller than that of (2,1)X. This is because (2,1)Z occupies smaller phase-space volume since it is isolated in the $\kappa \to 0$ limit. Thus the second shortest (2,1)X play major role also in the oblate side. However, the orbit (2,1)X reaches only up to $\delta \sim -0.2$ for $\kappa = 0.06$, and it cannot contribute much to the shell structures on the oblate side. At this realistic value of κ, the orbit (2,1)L causes a bifurcation from which triangular-type orbits (3,1) emerge as discussed above. With this bifurcation enhancement effect, their contribution to the shell energy become dominant on the oblate side. As one sees in the upper panel of figure 26, the constant-action lines of (2,1)L+(3,1) nicely explain the flat valleys in shell energy on the oblate side. For $\kappa = 0.03$, the half of the realistic value, the shell energy valleys are explained by the orbit (2,1)X on both prolate and oblate sides. Those valleys may play roles in establishing good oblate and prolate minima, and explain the reason for the disappearance of prolate dominance at this value of κ. In this way, the change in prolate-oblate asymmetry with varying spin-orbit coupling can be clearly understood from the properties of the classical POs.

In summary, we consider the behavior of the shell energy valleys in the (δ, N) plane which provides us the key to understand the origin of prolate-shape dominance in nuclear ground-state deformations. These shell energy valleys have large slopes on the prolate side while they are approximately flat in the oblate side, and one has less possibility to acquire shell energy gains

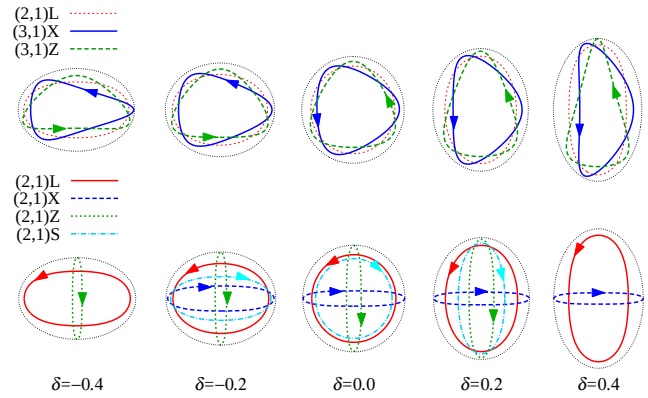


Figure 30. Some shortest meridian orbits for the power parameter $\alpha = 5.0$ and the spin-orbit parameter $\kappa = 0.06$ with several values of the deformation parameter δ. The orbit (2,1)S causes pair annihilations with (2,1)X at $\delta = -0.23$, and with (2,1)Z at $\delta = 0.23$.

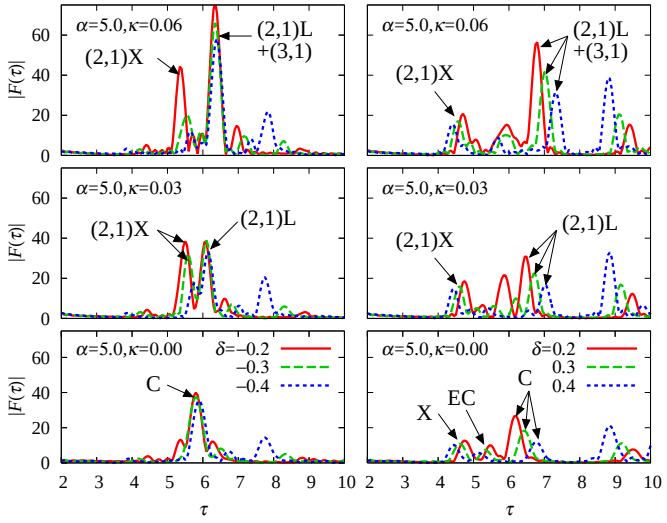


Figure 31. Comparison of the quantum Fourier spectra $|F^{\rm qm}(\tau;\delta)|$ plotted for several values of the deformation parameter δ on the oblate (left panels) and prolate (right panels) sides. Bottom, middle and top panels are the results for the spin-orbit parameter $\kappa = 0.00$, 0.03 and 0.06, respectively, with the power parameter $\alpha = 5.0$.

with oblate deformations. In practice, one sees nice correspondence between the properties of the valley slopes and the deformed shell-energy gains. The features of the level fannings should also have some effects but seems to bear less important roles in the gross shell effects. The way in which POs contribute to the shell energy is quite sensitive to the spin-orbit parameter. Although the shell energy valleys for $\kappa = 0$ look similar to the case of realistic value $\kappa = 0.06$, the semiclassical mechanisms for the enhancement of the PO contributions are quite different in both cases. Thus, above semiclassical interpretation gives us a deeper understanding on the origin of prolate dominance for realistic nuclear systems.

7. Conclusions and perspectives

Applying the semiclassical POT to the radial power-law potential models, emergence of a rich variety of nuclear shell structures are investigated from the view point of quantum-classical correspondence. In our semiclassical analyses, we make full use of the scaling properties of the power-law potential model and the Fourier transformation techniques, which are also effective under the existence of spin-orbit coupling. We have emphasized the significant roles of the PO bifurcations for the remarkable enhancement of shell effects with varying the parameters like surface diffuseness (controlled by the power parameter α), deformations and spin-orbit coupling strength. At the bifurcation points, a family of quasi-periodic orbits appears around the bifurcating PO, where an approximate dynamical symmetry is locally restored. In the bridge-orbit bifurcation, the above local family occupies a large volume of the phase-space extending along the trail of the bridge which connects two widely separated POs, and brings about a larger dynamical symmetry compared to those for simple bifurcations. We have found such peculiar bridge-orbit bifurcations play pivotal roles in exotic nuclear deformations such as superdeformations and tetrahedral deformations. It is also interesting to note that, the SU(3) symmetry of the spherical HO Hamiltonian, once broken for sharp potential surface with power parameter $\alpha > 2$, is partially compensated by the spin-orbit coupling as we see in section 4, and also by the octupole deformation of Y_{32} type as we see in section 5.2. Semiclassical analyses based on the realistic model for nuclear mean field with spin-orbit coupling taken into account provide us a deep understanding of the origin of the prolate-shape dominance, which may show up under a delicate balance between the effect from the surface diffuseness and that from the spin-orbit coupling.

Analyses of other types of nuclear deformations using the power-law potential model with and without spin-orbit coupling are also intended. For instance, properties of shell structure under reflection-asymmetric shapes by considering combinations of different types of the octupole deformations, also with the quadrupole terms, should be interesting, which might be responsible for the systematics of ground-state deformations with reflection asymmetry, and also for the fragment mass asymmetries in nuclear fissions.

In this paper, we have used the semiclassical trace formula to extract information on contributing classical POs from the quantum-mechanically calculated single-particle spectra by means of the Fourier transformation technique and the methods of constant-action lines, but have not directly estimated the semiclassical level densities and shell energies in the bifurcation region. It is a challenging subject to develop analytic and numerical methods to evaluate semiclassical trace formula valid under existence of continuous symmetries, bifurcations, and coupling with spin degree of freedom. This becomes actually important when we apply the semiclassical theories to more general Hamiltonians without scaling, which would be required, for instance, in descriptions of weekly bound nuclei. Concerning the shell structures of such unstable nuclei, quenching of the spherical shell gaps might be one of the interesting subjects [61].

Acknowledgments

The author thanks K. Matsuyanagi for discussions, comments and careful reading of the manuscript.

Appendix: Analyses of periodic orbit bifurcations with monodromy matrices

Classical PO changes their shapes continuously with varying potential parameter. The monodromy matrix (37) varies accordingly and one of the eigenvalues may coincides with unity which causes a bifurcation the orbit. Due to the symplectic property of the Hamiltonian dynamics, the monodromy matrix M is real and symplectic:

$$M^T J M = J, \quad J = \begin{pmatrix} 0 & -I \\ I & 0 \end{pmatrix}. \tag{A1}$$

Hence, the eigenvalues of M always appear in a conjugate-reciprocal pair either of

(i) $\mathrm{e}^{\pm \mathrm{i}v}$ with real v (elliptic)

(ii) $\mathrm{e}^{\pm u}$ with real u (hyperbolic)

(iii) $-\mathrm{e}^{\pm u}$ with real u (hyperbolic with reflection)

or in a quartet

(iv) $e^{\pm u \pm \mathrm{i}v}$ with real u and v (loxodromic).

The bifurcation takes place at $v = 0$ in the case (i) or at $u = 0$ in the case (ii). The POs are stable if the monodromy matrix has only elliptic eigenvalues, and otherwise unstable because the deviations of the initial condition will grow exponentially as time evolves.

For the 2D systems, or the 3D systems with axial symmetry, generic PO has a (2×2) (symmetry reduced) monodromy matrix and its eigenvalues appear in a pair either of (i)–(iii). The stability of a PO is uniquely determined by the value of the stability factor $t = \mathrm{Tr}\, M - 2 = -\det(M - I)$ as

(i) $t = 2\cos v - 2 = -4\sin^2(v/2), \quad -4 \le t \le 0$

(ii) $t = 2\cosh u - 2 = 4\sinh^2(u/2) > 0$

(iii) $t = -2\cosh u - 2 = -4\cosh^2(u/2) < -4$

For 3D systems without continuous symmetry, generic PO has (4×4) monodromy matrix, and its four eigenvalues can be generally expressed as $(\lambda_1, \lambda_1^{-1}, \lambda_2, \lambda_2^{-1})$. Then the stability of the PO is determined by the two stability factors t_i $(i = 1, 2)$ defined by

$$t_i \equiv \lambda_i + \lambda_i^{-1} - 2 = -(\lambda_i - 1)(\lambda_i^{-1} - 1). \tag{A2}$$

With the relations

$$\mathrm{Tr}(M - I) = t_1 + t_2, \quad \det(M - I) = t_1 t_2, \tag{A3}$$

the above stability factors are simply obtained as the two roots of the quadratic equation

$$t^2 - t\,\mathrm{Tr}(M - I) + \det(M - I) = 0. \tag{A4}$$

If the monodromy matrix has two pairs of eigenvalues either in (i)–(iii) above, both t_1 and t_2 take the real values as in 2D cases, while they take complex values $t_1, t_2 = t_1^*$ for the loxodromic case (iv).

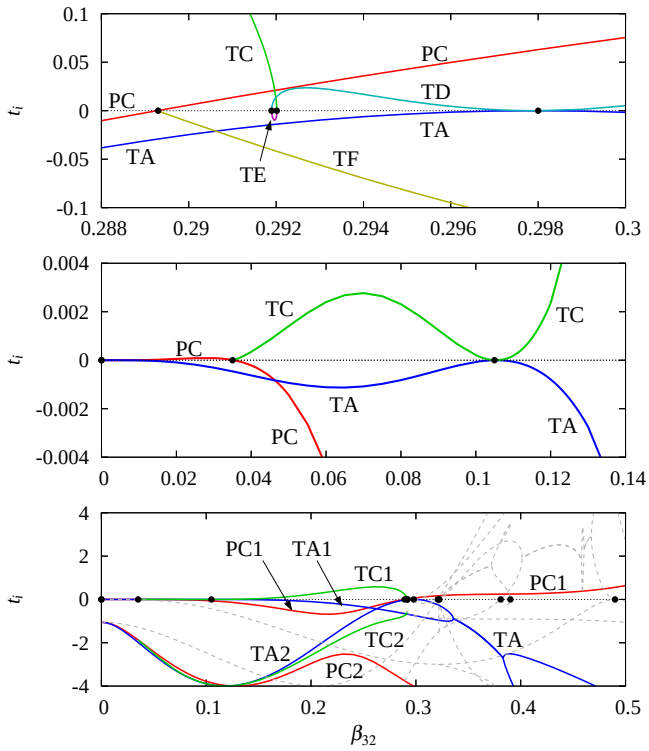


Figure 32. Stability factors t_i (or $\mathrm{Re}\, t_i$ for loxodromic stability) of some shortest POs as functions of the octupole deformation parameter β_{32}. Dots indicate the bifurcation points.

As the first example, we shall discuss some details on the bifurcations found in the power-law potential with Y_{32} deformation which we discussed in section 5.2. The planar triangular orbit PC, and 3D triangular orbits TA and TC (see figure 21) play the most important roles in deformed shell structure. Figure 32 displays the values of t_i for some shortest POs as functions of the deformation parameter β_{32}. As one sees in the bottom panel, one of the t_i's for the above three dominant POs are very close to zero in $0 < \beta_{32} < 0.3$, and those POs undergo bifurcations almost simultaneously at $\beta_{32} \sim 0.3$, where deformed shell effect is extremely enhanced. In the middle panel, expanded plots of those POs in the small β_{32} region are shown. The planar orbit PC undergoes pitchfork bifurcation at $\beta_{32} = 0.035$ and the 3D orbit TC emerges. TC and TA undergo touch-and-go bifurcation at $\beta_{32} = 0.105$. In the top panel, expanded plots around the bifurcation deformation $\beta_{32} \sim 0.29$ are shown. The orbit PC undergoes pitchfork bifurcation at $\beta_{32} = 0.289$ and 3D orbit TF emerges. A pair of 3D orbits TD and TE emerge via tangent bifurcation at $\beta_{32} = 0.292$, and TE causes a pair annihilation with TC just after its emergence. The orbits TD and TA undergo touch-and-go bifurcation at $\beta_{32} = 0.298$. As described here, the above dominant POs are connected with each other by the complicated network of quasi-periodic families of orbits via bifurcations. This feature seems peculiar to the tetrahedral-type deformations [55].

For the second example, let us discuss the bifurcations of the orbits (2,1) in spheroidal power-law potential with spin-orbit coupling which we discussed in section 6. We limit ourselves to

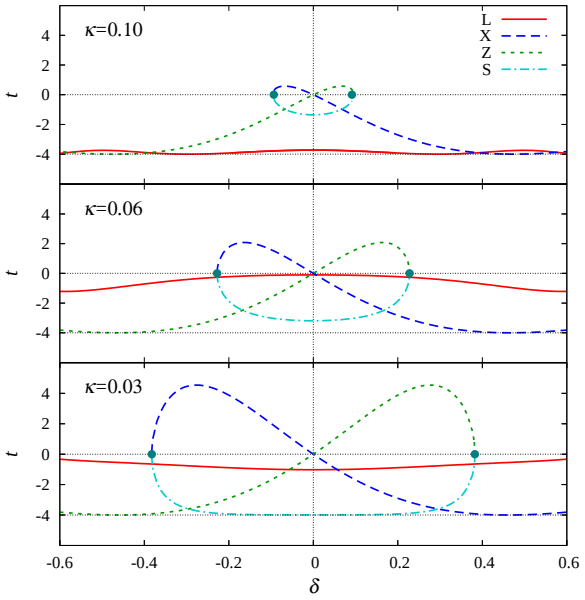


Figure 33. The stability factor t of the frozen-spin meridian orbits (2,1)L, (2,1)X, (2,1)Z and (2,1)S in spheroidal power-law potential as functions of the deformation parameter δ. The results for the power parameter $\alpha = 5.0$ with three different values of the spin-orbit parameter $\kappa = 0.03$, 0.06 and 0.10 are shown. Dots indicate the bifurcation points of (2,1)S.

the frozen-spin orbits in the meridian plane, and only consider the bifurcation within a given meridian plane, e.g. the (x, z) plane. Under this limitation, bifurcations of POs can be considered in terms of the reduced (2×2) monodromy matrix M. Figure 33 shows the values of the stability factor $t = \mathrm{Tr}(M - I)$ for four oval-shape orbits (2,1) as functions of spheroidal deformation parameter δ. For the spherical shape $\delta = 0$, the orbits X and Z compose the same degenerate family. With increasing oblate deformation $\delta < 0$, orbit (2,1)X approaches (2,1)S and they finally cause pair annihilation via tangent bifurcation at the certain deformation $\delta = -\delta_c$. With increasing prolate deformation $\delta > 0$, the orbit (2,1)Z approaches (2,1)S and they cause pair annihilation via tangent bifurcation at $\delta = \delta_c$. The value of δ_c becomes smaller as increasing spin-orbit parameter κ. The value of t for the orbit (2,1)L at $|\delta| \lesssim 0.2$ is very close to zero for $\kappa = 0.06$ since the orbit is close to the bifurcation point from which the orbits (3,1) emerge. This indicates that the (3,1) bifurcation makes significant effect on the deformed shell structure for the realistic spin-orbit strength $\kappa = 0.06$ in rather wide range of the deformation parameter δ.

References

[1] Bohr A and Mottelson B R 1969 *Nuclear Physics* vol 1 (New York: Benjamin)
Bohr A and Mottelson B R 1975 *Nuclear Physics* vol 2 (New York: Benjamin)

[2] Ring P and Schuck P 1980 *The Nuclear Many-Body Problem* (New York: Springer-Verlag)

[3] Gutzwiller M C 1967 *J. Math. Phys.* **8** 1979
Gutzwiller M C 1971 *J. Math. Phys.* **12** 343

[4] Strutinsky V M 1967 *Nucl. Phys.* A **95** 420
Strutinsky V M 1968 *Nucl. Phys.* A **122** 1

[5] Brack M and Pauli C 1973 *Nucl. Phys.* A **207** 401

[6] Balian R and Bloch C 1972 *Ann. Phys. NY* **69** 76

[7] Brack M and Bhaduri R K 2003 *Semiclassical Physics* (Boulder: Westview Press)

[8] Berry M V and Mount K E 1972 *Rep. Prog. Phys.* **35** 315

[9] Schulman L S 1981 *Techniques and applications of path integration* (New York: Wiley)

[10] Strutinsky V M 1975 *Nukleonika* (Poland) **20** 679
Strutinsky V M, Magner A G 1976 *Sov. J. Par. Nucl.* **7** 138

[11] Strutinsky V M, Magner A G, Ofengenden S R and Døssing T 1977 *Z. Phys.* A **283** 269

[12] Nishioka H, Hansen K and Mottelson B R 1990 *Phys. Rev.* B **42** 9377

[13] Berry M V and Tabor M 1976 *Proc. R. Soc. Lond.* A **349** 101

[14] Creagh S and Littlejohn R G 1991 *Phys. Rev.* A **44** 836

[15] Ozorio de Almeida A M and Hannay J H 1987 *J. Phys.* A **20** 5873

[16] Ozorio de Almeida A M 1988 *Hamiltonian Systems: Chaos and Quantization* (Cambridge: Cambridge University Press)

[17] Arita K and Brack M 2008 *Phys. Rev.* E **77** 056211

[18] Sieber M, 1996 *J. Phys.* A **29** 4715

[19] Magner A G, Fedotkin S N, Arita K, Misu T, Matsuyanagi K, Schachner T and Brack M 1999 *Prog. Theor. Phys.* **102** 551

[20] Magner A G, Vlasenko A A and Arita K 2013 *Phys. Rev.* E **87** 062916

[21] Nilsson S G 1955 *Mat. Fys. Medd. Dan. Vid. Selsk.* **29** No.16

[22] Carbonell J, Brut F, Arview R and Touchard J 1985 *J. Phys.* G **11** 385
Arview R, Brut F and Carbonell J 1987 *Phys. Rev.* A **35** 2389

[23] Buck B and Pilt A 1977 *Nucl. Phys.* A **280** 133

[24] Arita K, 2012 *Phys. Rev.* C **86** 034317

[25] Cwiok S, Dudek J, Nazarewicz W, Skalski J and Werner T 1987 *Comp. Phys. Comm.* **46** 379

[26] Kuratsuji H and Suzuki T 1980 *J. Math. Phys.* **21** 472

[27] Pletyukhov M and Zaitsev O 2003 *J. Phys.* A **36** 5181

[28] Yabana H and Horiuchi H 1986 *Prog. Theor. Phys.* **75** 592
Yabana H and Horiuchi H 1987 *Prog. Theor. Phys.* **77** 517

[29] Littlejohn R G and Flynn W G 1991 *Phys. Rev.* A **44** 5239
Littlejohn R G and Flynn W G 1992 *Phhs. Rev.* A **45** 7697

[30] Frisk H and Ghur T 1993 *Ann. Phys.* **221** 229

[31] Amann Ch and Brack M 2002 *J. Phys.* A **35** 6009

[32] Bahri C, Draayer P J and Moszkowski S A 1992 *Phys. Rev. Lett.* **68** 2133

[33] Blokhin H, Bahri C and Draayer P J 1994 *Phys. Rev. Lett.* **74** 4149

[34] Bohr A, Hamamoto I and Mottelson B R 1982 *Phys. Scr.* **26** 267

[35] Dudek J, Nazarewicz W and Leander G A 1987 *Phys. Rev. Lett.* **59** 1405

[36] Nazarewicz W, Twin P J, Fallon P and Garrett J D 1990 *Phys. Rev. Lett.* **64** 1654

[37] Nolan P J and Twin P J 1988 *Ann. Rev. Nucl. Part. Sci.* **38** 533

[38] Janssens R V F and Khoo T L 1991 *Ann. Rev. Nucl. Part. Sci.* **41** 321

[39] Brack M, Damgaard J, Jensen A S, Pauli H C, Strutinsky V M and Wong C Y 1972 *Rev. Mod. Phys.* **44** 320

[40] Bjornholm S and Lynn J E 1980 *Rev. Mod. Phys.* **52** 725

[41] Dudek J, Pomorski K, Schunck N and Dubray N 2004 *Eur. Phys. J.* A **20** 15

[42] Arita K and Brack M 2008 *J. of Phys.* A **41** 385207

[43] Magner A G, Arita K, Fedotkin S N and Matsuyanagi K 2002 *Prog. Theor. Phys.* **108** 853

[44] Arita K, 2004 *Int. J. Mod. Phys.* E **13** 191

[45] Butler P A and Nazarewicz W 1996 *Rev. Mod. Phys.* **68** 349

[46] Tagami S, Shimizu Y R and Dudek J 2012 *Prog. Theor. Phys. Suppl.* **196** 334
Tagami S, Shimizu Y R and Dudek J 2013 *Phys. Rev.* C **87** 054306

[47] Gustafsson C, Möller P and Nilsson S G 1971 *Phys. Lett.* B **34** 349

[48] Brack M, Reimann S M and Sieber M 1997 *Phys. Rev. Lett.* **79** 1817
Brack M, Sieber M and Reimann S M 2001 *Phys. Scr.* T **90** 146

[49] Hamamoto I, Mottelson B R, Xie H and Zhang X Z 1991 *Z. Phys.* D **21** 163

[50] Takami S, Yabana K and Matsuo M 1998 *Phys. Lett.* B **431** 242

[51] Dudek J, Goźdź A, Schunck N and Miśkiewicz M 2002 *Phys. Rev. Lett.* **88** 252502

[52] Reimann S M *et al* 1997 *Phys. Rev.* B **56** 12147

[53] Landau L D and Lifshitz E M 1981 *Quantum Mechanics (Non-relativistic Theory)* (New York: Pergamon Press) Chap. XII

[54] Inui T, Tanabe Y and Onodera Y 1990 *Group Theory and Its Applications in Physics* (Berlin: Springer-Veralg)

[55] Arita K and Mukumoto Y 2014 *Phys. Rev.* C **89** 054308

[56] Tajima N, Takahara S and Onishi N 1996 *Nucl. Phys.* A **603** 23

[57] Frisk H, 1990 *Nucl. Phys.* A **511** 309

[58] Hamamoto I and Mottelson B R 2009 *Phys. Rev.* C **79** 034317

[59] Tajima N and Suzuki N 2001 *Phys. Rev.* C **64** 037301
Tajima N, Shimizu Y R and Suzuki N 2002 *Prog. Theor. Phys. Suppl.* **146** 628

[60] Takahara S, Tajima N and Shimizu Y R 2012 *Phys. Rev.* C **86** 064323

[61] Dobaczewski J, Hamamoto I, Nazarewicz W and Sheikh J A 1994 *Phys. Rev. Lett.* **72** 981